Transformation-induced plasticity in SMA composites experiencing fiber bridging phenomenon

Amin Ardali [a], Jafar Rouzegar [a,*], Soheil Mohammadi [b], Mina Karimi [c]

[a] *Department of Mechanical Engineering, Shiraz University of Technology, Shiraz, Iran*
[b] *School of Civil Engineering, College of Engineering, University of Tehran, Tehran, Iran*
[c] *Department of Civil and Environmental Engineering, Carnegie Mellon University, PA, 15213, United States*

ARTICLE INFO

ABSTRACT

The present study aims to investigate the fiber bridging phenomenon in the fracture of a composite sheet reinforced with shape memory alloy wires undergoing transformation-induced plasticity in pseudoelastic loading. To this end, the Entchev-Lagoudas thermomechanical model is used, and the necessary equations to describe the adiabatic conditions of nitinol fibers are extracted considering the transformation-induced plasticity. The formulation needed for the numerical implementation of the constitutive model of the shape memory alloy is then developed using the convex cutting plane algorithm. The force effect of the bridging fibers on the crack edges of the composite specimen is applied directly, and the extended finite element method is used to study the fracture of the cracked composite specimen. The present research examines the effects of temperature conditions, fiber volume fraction, matrix material, and residual stresses on the results.

1. Introduction

Shape memory alloy (SMA) materials have significant applications in engineering and medicine due to their unique characteristics, such as shape memory and pseudoelasticity effects [1,2]. Comprehensive understanding of the thermomechanical behavior of SMA would eventually improve its industrial and engineering applications. Unlike ordinary materials whose mechanical capabilities are not distinctly affected by the loading type, the SMA behavior is significantly influenced by the thermomechanical loading. Along with other factors such as the environmental conditions and the alloy composition, the type of loading can create one or more unique specifications, such as the one-way shape memory, the two-way shape memory, and the pseudoelasticity effects. In fact, each of these capabilities in the material is associated with a specific point in the stress-strain-temperature space.

In the shape memory effect, the main point is the extreme coupling of temperature with stress and strain, which causes the residual strain. This strain is usually assumed plastic and irreversible and could be recovered with the increased temperature. This property can be a two-way effect depending on the twin or simple martensitic variant of the alloy. The pseudoelasticity effect is another important property of SMAs, which makes them materials that can withstand high mechanical strains before reaching the plastic region. The point is that the loading and unloading responses do not follow the same path in the stress-strain curve, and a loop can be observed at the end of each pseudoelasticity cycle.

Several subjects should be addressed in expressing the fundamental thermomechanical equations of SMA. The first point is the extreme coupling between the temperature and mechanical responses; leading to the significant role of temperature in the shape memory effect of SMA.

Secondly, the differential scanning calorimeter (DSC) test on the nitinol sample shows that phase transformation from full austenitic phase to martensite is an exothermic process, but the phase transformation from martensite to austenite is endothermic. This property of SMA should be considered, especially in pseudoelasticity loadings. The exothermic transformation from the austenite to the martensite during the mechanical loading and the endothermic transformation from the martensite to the austenite during the unloading increases and decreases the temperature, respectively. If the loading (or unloading) rate is low enough, the process can be assumed to be almost isothermal due to the heat transfer through convection and conduction. However, the isothermal assumption is not possible at high loading and unloading rates, which require the adiabatic assumption for SMA fibers.

The third point in expressing the thermomechanical equation of SMAs is the transformation-induced plasticity (TRIP) which is a special type of plasticity induced by successive phase transformations. It is the result of stress or temperature changes in the pseudoelasticity and shape memory effects, respectively. Considering this type of plasticity is more

---

Nomenclature

a_h	Heaviside enrichment degrees of freedom
b_k^l	Crack tip enrichment degrees of freedom
c	Specific heat capacity
D_i^b	Parameters for the evolution of back stress
D_i^d	Parameters for the evolution of drag stress
f	Nodal force vector
f_i^a	Force vector components related to crack faces enrichment functions
f^b	Body force vector
$f_i^{b\alpha}$	Force vector components related to the crack tip enrichment functions
f_i^e	Components of elemental force vector
F_l	Crack tip enrichment functions
f^t	External traction vector
G	Specific Gibbs free energy
H	Heaviside function
H^{cur}	Maximum transformation strain at current stress
H^{cur-r}	Maximum current transformation strain at the reversal of forward transformation
k	Stiffness matrix
m	Number of enrichment functions
mt	Number of nodes to be enriched by crack tip enrichment functions
m_1	Parameter for the evolution of drag stress
M^{0s}	Material parameter
n	Sets of all finite element nodes
N_j	Finite element shape functions
P_i	Point forces of smart bridging fibers on the crack edges
q	Heat flux vector

r	Heat source
S	Compliance tensor
s_0	Specific entropy at reference state
T	Temperature
T_0	Reference temperature
u_0	Specific internal energy at the reference state
u_j	Nodal displacements (standard degrees of freedom)
u^h	Vector of degrees of nodal freedom (for both classical and enriched ones)
Y	Critical value for thermodynamic force to cause transformation
α	Thermal expansion coefficient tensor
β	Back stress tensor
γ	Minor loop parameter
ε	Infinitesimal strain tensor
ε^t	Transformation strain tensor
ε^p	Plastic strain tensor
ξ	Total martensitic volume fraction
ξ^d	Detwinned martensitic volume fraction
ξ^s	Distance function
ζ^d	Accumulated detwinned martensitic volume fraction
λ	Material constant that governs the increasing rate of $D_i^{b,d}$
η	Drag stress tensor
Λ	Transformation tensor
Λ^p	Transformation-induced plasticity tensor
π	Thermodynamic force
ρ	Mass density
Φ	Phase transformation function
σ	Stress tensor
σ^{eff}	Effective stress tensor

pronounced in cyclic loadings because the plastic strains of cycles are accumulated. The composition of SMA is one of the most important factors affecting the magnitude of plastic strain caused by the phase transformation. In some compounds, a stable and saturated state is achieved in the thermomechanical behavior of the material after a few loading cycles. But in others, saturation is not easily achieved. Therefore, TRIP effects should not be ignored in sensitive engineering structures. Studying the fracture of a mechanical structure aims to determine the boundary between its continuity and rupture. Thus, accurate modeling of the bridging effects of fibers on the crack edges in a composite specimen reinforced with SMA wires needs to consider the TRIP effect.

A number of experimental, analytical, and numerical studies on SMAs exist in the literature: Tanaka [1] described a constitutive model for SMAs by defining the following variables: strain, temperature, and martensitic volume fraction. Considering Gibbs free energy, Boyd and Lagoudas [2,3] proposed a constitutive model for the thermomechanical coupling response of SMA. Strnadel et al. [4] examined the mechanical properties of nickel-titanium alloys by performing experimental tests on laboratory specimens under the pseudoelasticity loadings. Liang and Rogers [5] estimated the martensitic volume fraction by a cosine function in the basic relations of the Tanaka model. Bo and Lagoudas [6] developed a thermomechanical model for the SMAs to estimate plastic strains at cyclic loadings. They estimated the plastic strain induced by the bidirectional shape memory effect. They also examined a parameter through which the energy dissipation in incomplete loading cycles of SMAs could be better estimated [7]. Yencho and Lagoudas [8,9] introduced a three-dimensional model based on Bo and Lagoudas model [6] to simulate the TRIP. The effect of cyclic loading on the thermomechanical properties of SMAs was experimentally investigated by Flor

et al. [10]. Yu and Young [11] tried to develop a new model for the constitutive equations governing the pseudoelastic behavior of SMA by considering the strain rate effect. Chemisky et al. [12] developed a three-dimensional model for the constitutive equations of SMAs under fatigue conditions.

Depending on the loading path, the use of SMA in the form of fibers or actuators in the bed of the host structure could lead to control of stiffness or shape of the structure. One of the studies conducted in this field is that of Birman et al. [13], who introduced a suitable distribution for the combined use of memory actuators and piezoelectric actuators. Using the finite element method, Roh and Kim [14] achieved results by placing SMA wires in the center of a multilayer composite structure. Khalili et al. [15,16] examined the dynamic analysis of polymer plates reinforced with shape-memory wires. Daghia et al. [17] adopted the finite element method to work on the stiffness and shape control of composite sheets reinforced with SMA and compared the results with the experimental data. Jarali and Raja [18] developed a new model to investigate the stress distribution at the interface of smart nitinol fibers and composite matrix. Freed and Aboudi [19] conducted an analytical study on the TRIP effect of shape memory fibers in smart composites. Oehler et al. [20] examined the optimization of a morphing structure activated by woven nitinol wires. The analysis of thin double-curved smart composite shells subjected to low-velocity transverse impact loading was carried out by Khalili and Ardali [21]. Bahrami et al. [22,23] investigated the fracture of SMAs through the finite element method by their proposed constitutive equations. Karakalas et al. [24] numerically simulated the damping capacity of SMAs under adiabatic and heat transfer conditions.

Fibers bridging across a crack may force the crack edges to get closer to each other due to temperature changes or pseudoelasticity properties.

Several investigations have been performed on these phenomena for analysis of structures reinforced with SMA. Hamada et al. [25] investigated the shape memory effect of smart fibers on crack healing in composites. Using the finite element method, Wang et al. [26] investigated the stress distribution around the crack tip of an SMA under pseudoelasticity loading. Burton et al. [27] simulated the behavior of the composites reinforced with the self-healing SMAs by the finite element method. Lexcellent and Thiebaud [28] examined the behavior of the phase transformation zone at the crack tip of an SMA under asymmetric tensile and compressive loadings. Desindes and Daly [29] studied the
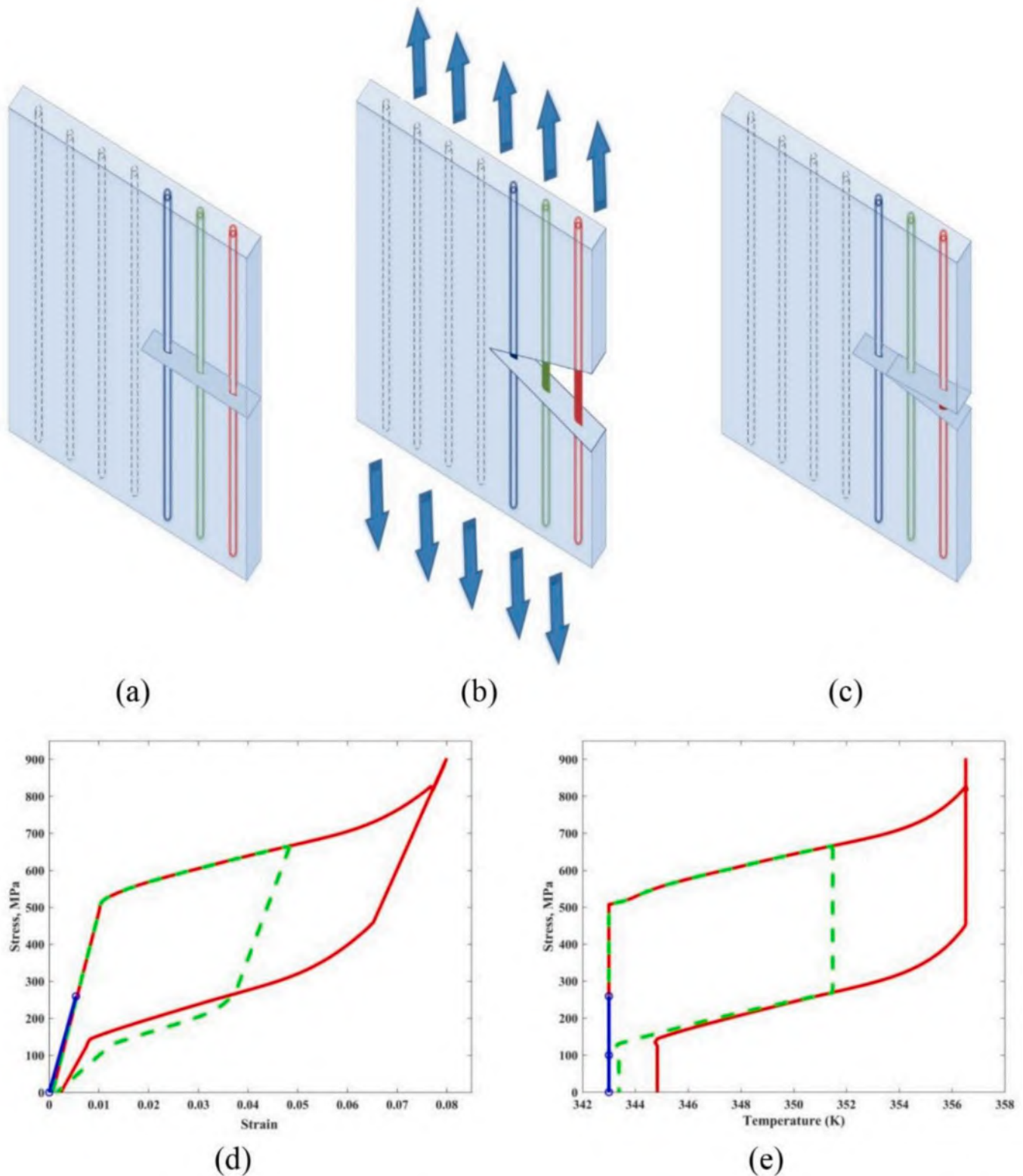

Fig. 1. (a,b,c) Schematic presentation of fiber bridging in the crack path; the initial state, the loading, and the finally unloading ones, respectively. (d,e) Thermomechanical behavior of bridging fibers experiencing TRIP; the stress-strain-temperature responses.

fracture of SMAs under the mode III loading and the small-scale yielding condition. Maletta and Furgiuele [30] investigated the parameters affecting the crack tip stress field in SMAs under pseudoelasticity loading at different temperatures. Ferguson et al. [31] studied the effect of SMA wires and their quasi-plastic strain recovery due to temperature increases on the damaged surfaces. Cohades et al. [32] conducted an experimental study on polymer composites to investigate the effect of nitinol fibers on microcrack healing due to impact loading. Afshar et al. [33] examined the effect of the fiber bridging phenomenon in combined fracture modes using the extended finite element method. On the other hand, Karimi et al. [34] analyzed the crack healing process in composites reinforced with SMA fibers. They found that the effect of nitinol fibers' shape memory and the restoration of their original shape subjected to the increasing temperature could improve the crack healing mechanism in the composite structure. Mirsayar and Hartl [35] addressed the crack propagation in the composite matrix and perpendicular to the SMA fibers. Ardakani et al. [36] numerically analyzed the delamination in bi-material composites containing SMA and elastoplastic layers. Another study by Mirsayar and Hartl [37] dealt with the mixed-mode fracture in notched SMA structures using the thermomechanical constitutive modeling of shape memory alloys [38] and the strain energy density criterion.

In the present study, the property of superelasticity of SMAs in the fiber bridging mechanism across a crack is examined for the first time. In addition, the effects of TRIP of nitinol fibers on the fracture of composite specimens are addressed. Given that the temperature-stress-strain coupling in SMA alloys is especially important in high loading rates, formulations associated with the adiabatic conditions of the fibers in the TRIP mode are extracted through the Lagoudas constitutive model. In order to achieve a simpler numerical algorithm, the equations required for the convex cutting plane algorithm are numerically implemented. The effects of smart fibers are applied as force actuators to the composite crack edges through the use of the Entchev-Lagoudas constitutive model. The extended finite element method (XFEM) is utilized for modeling the problem. The crack length is kept constant in this paper. What follows is a brief presentation of the constitutive equations of the SMAs under the TRIP condition. Then, the XFEM formulation for modeling the cracked composite specimen is presented. Finally, the results are compared in three parts including the monolithic alloy as well as the smart composites with elastomeric and aluminium matrices.

2. Theory and formulation

Fig. 1 schematically shows the three stages of the initial state, the loading, and the final unloading of a two-dimensional crack with the bridging fibers with the thermomechanical characteristics presented in Table 1 in three different colors. The locations of the blue, green, and red fibers are respectively closer to the tip of the crack. Fibers farther from the crack tip (red fibers in Fig. 1) experience longer crack openings and are more likely to undergo complete martensitic transformation. Some fibers (green fibers in Fig. 1) may not experience a complete cycle of phase transformation and consequently, minor loops occur for them. In addition, there might be some fibers (blue fibers in Fig. 1) that are completely in the linear elastic region and do not experience any phase transformations. Clearly, different conditions may occur for these fibers in terms of the irreversible strains and temperature changes. In addition, the type of material used as the matrix phase in the composite is very important, which may affect the overall behavior of SMA fibers. In this research, aluminium and elastomeric matrices are used to study the behavior of cracked composite specimens reinforced with the SMA wires.

2.1. Thermomechanical coupled constitutive model of SMA under TRIP

The model used in this paper is the Lagoudas model [38], which works based on the first and second laws of thermodynamics and the

Table 1
Material parameters of Ti-49.7 at. %Ni alloy (wire diameter: 2.16 mm) [39].

Parameters remaining constant during the cyclic loading	$E^A = 52.0$ GPa	$E^M = 30.0$ GPa	$\nu = 0.33$
	$m_1 = 3.5$	$\gamma = 3.5$	$\alpha^A = 11.0 \times 10^{-6}$ K^{-1}
	$\alpha^M = 6.0 \times 10^{-6}$ K^{-1}	$\rho c^A = 2.12$ MJ/ (m^{3}K)	$\rho c^M = 2.12$ MJ/ (m^{3}K)
Parameters characterizing the response during the cyclic loading	$C_1^p = 1.0 \times 10^{-3}$	$C_2^p = 10.0$	$\lambda_1 = 0.1$
Parameters changing during the transformation cycling	Initial set	Final set	
	$M^{0s} = 309.0$ K	$M^{0s} = 309.0$ K	
	$H^{max} = 0.048$	$H^{max} = 0.042$	
	$\rho \Delta s_0 = -0.77$ MJ/(m^{3}K)	$\rho \Delta s_0 = -0.23$ MJ/(m^{3}K)	
	$Y = 11.0$ MJ/m^3	$Y = 4.7$ MJ/m^3	
	$D_1^d = 1.0$ MPa	$D_1^d = 10.0$ MPa	
	$D_2^d = 0.7$ MPa	$D_2^d = 0.5$ MPa	
	$D_1^b = 4.89 \times 10^3$	$D_1^b = 5.59 \times 10^3$	
	$D_2^b = -4.62 \times 10^5$	$D_2^b = -6.03 \times 10^5$	
	$D_3^b = 2.47 \times 10^7$	$D_3^b = 3.69 \times 10^7$	
	$D_4^b = -6.39 \times 10^8$	$D_4^b = -1.09 \times 10^9$	
	$D_5^b = 6.30 \times 10^9$ MPa	$D_5^b = 1.23 \times 10^{10}$ MPa	
The transformation temperatures of the untrained NiTi wire (for first cycle)	$M_s = 309$ K	$A_s^t = 313$ K ($M^t \rightarrow A$)	
	$M_f = 276$ K	$A_f^t = 333$ K ($M^t \rightarrow A$)	

Gibbs free energy defined by three independent variables of temperature, stress, and martensitic volume fraction. The Clausius-Planck inequality determines the possibility of a thermodynamic path

$$-\rho \frac{\partial G}{\partial \xi} \xi - \rho \frac{\partial G}{\partial \varepsilon^t} : \Lambda \dot{\xi} - \rho \frac{\partial G}{\partial \varepsilon^p} : \Lambda^p \dot{\xi} = \pi \dot{\xi} \geq 0 \tag{1}$$

where G is the Gibbs free energy, ξ is the martensitic volume fraction, ε^t and ε^p are the transformation strain tensor and the plastic strain tensor respectively, ρ is the mass density, Λ is the transformation tensor, Λ^p is the TRIP tensor and π is the thermodynamic force. In the case of the TRIP condition, the thermodynamic force is given by [39]

$$\pi = \frac{1}{2}\sigma : \Delta S : \sigma + \sigma : \Delta\alpha(T - T_0) + \sigma : \Lambda + \beta : \Lambda + \sigma$$
$$: \Lambda^p + \eta - \rho\Delta c \left[T - T_0 - T\ln\left(\frac{T}{T_0}\right)\right] + \rho\Delta s_0(T - M^{0s}) + Y \tag{2}$$

in which β is the back stress with the polynomial function of degree 5 [39]

$$\beta = -\frac{3}{2}\frac{\varepsilon^t}{|\varepsilon^t|}\left[D_1^b(H^{cur}(\sigma)\xi)^{(1)} + D_2^b(H^{cur}(\sigma)\xi)^{(2)} + D_3^b(H^{cur}(\sigma)\xi)^{(3)} \right.$$
$$\left. + D_4^b(H^{cur}(\sigma)\xi)^{(4)} + D_5^b(H^{cur}(\sigma)\xi)^{(5)}\right] \tag{3}$$

and η is the drag stress, defined by

$$\eta = -D_1^d[-\ln(1-\xi)]^{\frac{1}{m_1}} + D_2^d\xi. \tag{4}$$

σ^{eff} is the effective stress tensor,

$$\sigma^{eff} = \sigma + \beta, \tag{5}$$

where σ is the stress tensor, α is the thermal expansion coefficient tensor, S is the compliance tensor, T and T_0 are the temperature and the reference temperature, respectively, H^{cur} is the maximum transformation strain at the current stress, s_0 is the specific entropy at the reference state and m_1, M^{0s}, D_i^b, D_i^d are material parameters.

In the Lagoudas model, the phase transformation is assumed to occur

when the thermodynamic force π reaches the critical value of Y. The martensitic phase transformation will take place whenever the thermodynamic force reaches a critical value [39]. Separating the critical value of the thermodynamic force from Eq. (2) is given by

$$\Phi = \begin{cases} \pi - Y & \text{whenever} \quad \dot{\xi} > 0, \\ -\pi - Y & \text{whenever} \quad \dot{\xi} < 0. \end{cases} \tag{6}$$

in which Φ is the phase transformation function. Matching the Clausius-Planck inequality with the Kuhn-Tucker condition [39] results in

$$\dot{\xi} \geq 0, \Phi \leq 0, \Phi\dot{\xi} = 0, \tag{7}$$

$$\dot{\xi} \leq 0, \Phi \leq 0, \Phi\dot{\xi} = 0. \tag{8}$$

Therefore, the $\Phi = 0$ condition determines if the material is in the martensitic phase transformation range.

The proposed constitutive model is adopted for 1D shape memory. During the uniaxial loadings in the x_1 direction, the stress has only one non-zero component. Hence, the stress components are as follows [39]:

$$\sigma_{11} = \sigma \neq 0, \sigma_{ij} = 0 \quad \text{for all other i, j.} \tag{9}$$

where σ is the uniaxial applied stress. Assuming an isochoric process, uniaxial strain can be expressed in terms of the plastic strain and the transformation strain [39].

$$\varepsilon_{11} = \varepsilon = S\sigma + \alpha(T - T_0) + \varepsilon^{t} + \varepsilon^{p}, \tag{10}$$

The evolution equations for the transformation and plastic strain become

$$\dot{\varepsilon}^{t} = \Lambda\dot{\xi}, \tag{11}$$

$$\dot{\varepsilon}^{p} = \Lambda^{p}\dot{\zeta}^{d} \tag{12}$$

The uniaxial components of the transformation and TRIP tensors are given by

$$\Lambda = \Lambda_{11} = \begin{cases} H^{cur}(\sigma)\dfrac{\sigma^{eff}}{|\sigma^{eff}|}; & \dot{\xi} > 0, \\[3mm] H^{cur-r}\dfrac{\varepsilon^{t}_{max}}{|\varepsilon^{t}_{max}|}; & \dot{\xi} < 0, \end{cases} \tag{13}$$

$$\Lambda^{p} = \Lambda^{p}_{11} = \begin{cases} C^{p}_1\dfrac{\sigma^{eff}}{|\sigma^{eff}|}e^{\frac{-\zeta^d}{C^p_2}}; & \dot{\xi} > 0, \\[3mm] C^{p}_1\dfrac{\varepsilon^{t}_{max}}{|\varepsilon^{t}_{max}|}e^{\frac{-\zeta^d}{C^p_2}}; & \dot{\xi} < 0, \end{cases} \tag{14}$$

where H^{cur-r} is the maximum current transformation strain at the reversal of forward transformation and C^{p}_i are the material parameters during the cyclic loading. ξ^d and ζ^d are the detwinned martensitic volume fraction and the accumulated detwinned martensitic volume fraction, respectively, which are defined as [39]

$$\zeta^{d} = \int_0^t |\dot{\xi}^{d}(\tau)| d\tau. \tag{15}$$

$$\xi^{d} = \frac{H^{cur}(\sigma)}{H^{max}}\xi \tag{16}$$

$$\varepsilon^{p} = C^{p}_1 C^{p}_2 \left(1 - e^{\frac{-\zeta^d}{C^p_2}}\right) \tag{17}$$

During the cyclic loadings, several thermomechanical properties of SMA change [40]. Accumulation of irreversible plastic strains leads to some changes in the residual loop and the hysteresis effect. However, the loops move towards saturation. Material parameters in SMA are divided

into two categories. The first category includes the parameters that remain constant during the thermomechanical cycles, and the latter includes the ones that change during the cyclic loadings and the corresponding phase transformations. These parameters are D^b_i, D^d_i, H^{max}, Y, $\rho\Delta s_0$, and M^{0s}. The evolution relationship between the cyclic loadings is as follows [39]

$$D^b_i = \left(D^b_i\right)^{fin} + \left(\left(D^b_i\right)^{init} - \left(D^b_i\right)^{fin}\right)e^{-\lambda_1\zeta^d} \tag{18}$$

$$D^d_i = \left(D^d_i\right)^{fin} + \left(\left(D^d_i\right)^{init} - \left(D^d_i\right)^{fin}\right)e^{-\lambda_2\zeta} \tag{19}$$

$$H^{max} = H^{fin} + \left(H^{init} - H^{fin}\right)e^{-\lambda_1\zeta^d} \tag{20}$$

$$Y = Y^{fin} + \left(Y^{init} - Y^{fin}\right)e^{-\lambda_2\zeta} \tag{21}$$

$$M^{0s} = \left(M^{0s}\right)^{fin} + \left(\left(M^{0s}\right)^{init} - \left(M^{0s}\right)^{fin}\right)e^{-\lambda_2\zeta} \tag{22}$$

$$\rho\Delta s_0 = (\rho\Delta s_0)^{fin} + \left((\rho\Delta s_0)^{init} - (\rho\Delta s_0)^{fin}\right)e^{-\lambda_2\zeta} \tag{23}$$

For stress-induced phase transformation with large values of the applied stress [39] (if, of course, $\lambda_1 = \lambda_2$)

$$\zeta = \zeta^{d} \tag{24}$$

The parameters affected by the martensitic volume fraction are as follows [39].

$$c(\xi) = c^{A} + \xi\Delta c \tag{25}$$

$$s_0(\xi) = s^{A}_0 + \xi\Delta s_0 \tag{26}$$

$$u_0(\xi) = u^{A}_0 + \xi\Delta u_0 \tag{27}$$

$$\alpha(\xi) = \alpha^{A} + \xi\Delta\alpha \tag{28}$$

$$S(\xi) = S^{A} + \xi\Delta S. \tag{29}$$

where c and u_0 are the specific heat capacity and the specific internal energy at the reference state, respectively. In general, the equation $(\Delta x = x^M - x^A)$ represents a parametric difference between the martensitic and the austenitic phases.

In many constitutive models describing the behavior of shape memory alloys, the phase transition temperatures appear in formulations, especially in hardening functions. While in the formulation of the Entchev-Lagoudas model, the back stress and the drag stress are used instead of the transformation hardening functions. According to the Entchev-Lagoudas model, the drag stress and the back stress are derived based on the materials parameters and the phase transition temperatures don't appear in the formulation because the phase transition temperatures may change during cycling due to the TRIP effect. In the Entchev-Lagoudas model, no explicit hardening function is included in this new form of Gibbs free energy, and the energetic consequences of phase mixing have been captured in the formulations of back and drag stresses.

2.2. Thermomechanical coupling in SMAs experiencing TRIP

It has been experimentally observed that the thermomechanical coupling in SMAs is strong. Considering that the latent heat is generated in the forward martensitic phase transformation and is absorbed in the reverse process, the mechanical behavior of the material is affected by the temperature changes. Therefore, modeling the thermomechanical coupling of nitinol alloy experiencing TRIP is a key requirement, especially during phase transformation.

The first step in modeling a thermomechanical coupling is to use the first law of thermodynamics (the principle of energy conservation). When this law is combined with the second law of thermodynamics (the

Clausius-Planck inequality) and the Legendre transformation [39],

$$\rho T\left(\frac{\alpha}{\rho}\dot{\sigma} + \frac{c}{T}\dot{T} + \left(\frac{1}{\rho}\Delta\alpha\sigma + \Delta c\, ln\left(\frac{T}{T_0}\right) + \Delta s_0\right)\dot{\xi}\right) = \pi\dot{\xi} - div(q) + \rho r \qquad (30)$$

where q and r are the heat flux vector and the heat source, respectively. The adiabatic heat transfer condition can be simulated by eliminating the right-hand side of the energy balance (heat) equation, $(- div(q) + \rho r = 0)$. Moreover, by assuming $\Delta\alpha = \Delta c = 0$, the heat equation assumes the form of [39]

$$(T\alpha : \dot{\sigma} + \rho c\dot{T} + (-\pi + T\Delta\alpha\sigma + \rho\Delta s_0 T)\dot{\xi}) = 0 \qquad (31)$$

On the other hand, the consistency condition requires that

$$\dot{\Phi} = \frac{\partial\Phi}{\partial\sigma} : \dot{\sigma} + \frac{\partial\Phi}{\partial T}\dot{T} + \frac{\partial\Phi}{\partial\xi}\dot{\xi} = 0 \qquad (32)$$

For forward (austenite to martensite with a positive sign) and reverse (martensite to austenite with a negative sign) phase transformations, the evolutionary terms are extracted from Eqs. (1) and (2), as follows

$$\frac{\partial\Phi}{\partial\sigma} = \pm\Delta S : \sigma \pm \Lambda \pm \Lambda^p \qquad (33)$$

$$\frac{\partial\Phi}{\partial T} = \pm\Delta\alpha : \sigma \pm \rho\Delta s_0 \qquad (34)$$

$$\frac{\partial\Phi}{\partial\xi} = \pm\frac{\partial\beta}{\partial\xi}\Lambda \pm \frac{\partial\eta}{\partial\xi} \qquad (35)$$

By putting Eqs. 33–35 in the consistency Eq. (32) for both forward and reverse phase transformations,

$$\dot{\xi} = -\frac{\Delta S : \sigma + \Lambda + \Lambda^p}{\frac{\partial\beta}{\partial\xi}\Lambda + \frac{\partial\eta}{\partial\xi}} : \dot{\sigma} - \frac{\Delta\alpha : \sigma + \rho\Delta s_0}{\frac{\partial\beta}{\partial\xi}\Lambda + \frac{\partial\eta}{\partial\xi}}\dot{T} \qquad (36)$$

and using $\dot{\xi}$ in the second thermodynamic Eq. (31),

$$\dot{T}_{fwd/rev} = -\frac{T\alpha - \chi}{\rho c - \delta} : \dot{\sigma} \qquad (37)$$

where

$$\chi = \frac{(-\pi + T\Delta\alpha\sigma + \rho\Delta s_0 T)(\Delta S : \sigma + \Lambda + \Lambda^p)}{\frac{\partial\beta}{\partial\xi}\Lambda + \frac{\partial\eta}{\partial\xi}} \qquad (38)$$

and

$$\delta = \frac{(-\pi + T\Delta\alpha\sigma + \rho\Delta s_0 T)(\Delta\alpha : \sigma + \rho\Delta s_0)}{\frac{\partial\beta}{\partial\xi}\Lambda + \frac{\partial\eta}{\partial\xi}} \qquad (39)$$

$\frac{\partial\beta}{\partial\xi}$ and $\frac{\partial\eta}{\partial\xi}$ are obtained from Eqs. (3) and (4)

$$\frac{\partial\beta}{\partial\xi} = -\frac{3}{2}\frac{\varepsilon^t}{|\varepsilon^t|}\Big[D_1^b(H^{cur}(\sigma))^{(1)} + 2D_2^b(H^{cur}(\sigma))^{(2)}\xi + 3D_3^b(H^{cur}(\sigma))^{(3)}\xi^2 \\ + 4D_4^b(H^{cur}(\sigma))^{(4)}\xi^3 + 5D_5^b(H^{cur}(\sigma))^{(5)}\xi^4\Big] \qquad (40)$$

$$\frac{\partial\eta}{\partial\xi} = -\frac{D_1^d}{m_1(1-\xi)}[-ln(1-\xi)]^{\left(\frac{1}{m_1}-1\right)} + D_2^d \qquad (41)$$

2.3. Numerical implementation of an SMA thermomechanical constitutive model under TRIP

Considering the three independent variables of temperature, stress, and martensitic volume fraction in the Gibbs free energy, the thermodynamic function obtained from the first and second laws of thermodynamics finally leads to Kuhn-Tucker conditions, which could predict the evolution path in the stress-strain-temperature diagrams by considering the martensitic transformation. These principles are considered in the Lagoudas model in order to achieve an accurate constitutive model of SMA [38]. To the best knowledge of the authors, no numerical implementation with the convex cutting plane explicit algorithm has been reported for the TRIP case, so far. The convex cutting plane method is based on the explicit integration of the differential equations, and its advantage lies in its simplicity and reduction in computations. It is based on the explicit integration of the transformation evolution equation from the thermoelastic predictor. The satisfaction of the transformation condition requires the use of Newton's iteration method. The convergence of the algorithm toward the final value of the state variables is obtained at a quadratic rate. Forward Euler integration makes the load-stepping procedure first-order accurate. One of the fundamental advantages of this method is its simplicity, which does not require computation of the gradient of the transformation tensor or inversion of algorithmic tangent tensors, and only involves a few tensorial operations and function evaluations to determine the unknowns.

This section deals with the development and implementation of the required relations based on the convex cutting plane explicit algorithm. This method works based on the concept of transformation correction. The problem inputs, namely temperature and strain, are considered predictor/corrector data that leads to the generation of predictor/corrector values for stress. The martensitic volume fraction changes until the Kuhn-Tucker conditions are met. In iterative cycles of transformation correction step, the total temperature and strain remain constant while other parameters change. The incremental-iterative form of the discretized evolution Eqs. (11) and (12) are given [39]:

$$\varepsilon^{t(k+1)}_{n+1} = \varepsilon^t_n + \left(\xi^{(k+1)}_{n+1} - \xi_n\right)\Lambda^t\left(\sigma^{(k+1)}_{n+1}\right) \qquad (42)$$

$$\varepsilon^{p(k+1)}_{n+1} = \varepsilon^p_n + \left(\xi^{d(k+1)}_{n+1} - \xi^d_n\right)\Lambda^p\left(\sigma^{(k+1)}_{n+1}\right) \qquad (43)$$

where n and k denote the time step and iteration counter, respectively. Introducing the iterative update and rearranging the above equations leads to

$$\Delta\varepsilon^{t(k)}_{n+1} = \Delta\xi^{(k)}_{n+1}\Lambda^t_{n+1}\left(\sigma^{(k)}_{n+1}\right) \qquad (44)$$

$$\Delta\varepsilon^{p(k)}_{n+1} = \Delta\xi^{d(k)}_{n+1}\Lambda^p_{n+1}\left(\sigma^{(k)}_{n+1}\right) \qquad (45)$$

$$d\varepsilon = d\varepsilon^e + d\varepsilon^{th} + d\varepsilon^t + d\varepsilon^p = Sd\sigma + \sigma dS + \alpha dT + \Lambda^t d\xi + \Lambda^p d\xi \qquad (46)$$

During the iterations, the current total strain and temperature are held constant $(d\varepsilon = \alpha dT = 0)$, so

$$\Delta\sigma^{(k)}_{n+1} = C^{(k)}_{n+1}\left[-\left(\Delta S\sigma^{(k)}_{n+1} + \Lambda^{t(k)}_{n+1}\right)\Delta\xi^{(k)}_{n+1} - \Lambda^{p(k)}_{n+1}\Delta\left|\xi^{d(k)}_{n+1} - \xi^d_n\right|\right] \qquad (47)$$

$$\Delta\sigma^{(k)}_{n+1} = -C^{(k)}_{n+1}\left[\Delta S\sigma^{(k)}_{n+1} + \Lambda^{t(k)}_{n+1} + \Lambda^{p(k)}_{n+1}sgn\left(\left(\frac{H^{cur}\xi}{H}\right)^{(k)}_{n+1} - \left(\frac{H^{cur}\xi}{H}\right)_n\right)\frac{H^{cur}}{H}\right]\Delta\xi^{(k)}_{n+1} \qquad (48)$$

The transformation function $\Phi^t(\sigma, \xi)$ in the next iteration is determined from

$$\Phi^{t(k)}_{n+1} + \Delta \Phi^{t(k)}_{n+1} = \Phi^{t(k+1)}_{n+1} \cong 0 \qquad (49)$$

Applying the chain rule [39].

$$\Phi^{t(k)}_{n+1} + \frac{\partial \Phi^{t(k)}_{n+1}}{\partial \sigma} : \Delta \sigma^{(k)}_{n+1} + \frac{\partial \Phi^{t(k)}_{n+1}}{\partial \xi} : \Delta \xi^{(k)}_{n+1} \cong 0 \qquad (50)$$

and substituting the stress increment defined in Eq. (48) into Eq. (50) leads to

Table 2
Cutting plane return mapping algorithm for the SMA constitutive model considering the TRIP effect under the adiabatic condition.

$$\Phi^{t(k)}_{n+1} - \frac{\partial \Phi^{t(k)}_{n+1}}{\partial \sigma} : C^{(k)}_{n+1}\left[\Delta S\sigma^{(k)}_{n+1} + \Lambda^{t(k)}_{n+1} + \Lambda^{p(k)}_{n+1} sgn\left(\left(\frac{H^{cur}\xi}{H}\right)^{(k)}_{n+1} - \left(\frac{H^{cur}\xi}{H}\right)_{n}\right)\frac{H^{cur}}{H}\right]\Delta\xi^{(k)}_{n+1} + \frac{\partial \Phi^{t(k)}_{n+1}}{\partial \xi} : \Delta\xi^{(k)}_{n+1} \cong 0 \tag{51}$$

Solving Eq. (51) yields

$$\Delta\xi^{(k)}_{n+1} = \frac{-\Phi^{t(k)}_{n+1}}{B^t_2} \tag{52}$$

$$B^t_2 = \frac{\partial \Phi^{t(k)}_{n+1}}{\partial \xi} - \frac{\partial \Phi^{t(k)}_{n+1}}{\partial \sigma} : C^{(k)}_{n+1}\left[\Delta S\sigma^{(k)}_{n+1} + \Lambda^{t(k)}_{n+1} + \Lambda^{p(k)}_{n+1} sgn\left(\left(\frac{H^{cur}\xi}{H}\right)^{(k)}_{n+1} - \left(\frac{H^{cur}\xi}{H}\right)_{n}\right)\frac{H^{cur}}{H}\right] \tag{53}$$

By introducing the notation of '±' where ' + ' and ' − ' correspond to forward and reverse phase transformation, respectively, one obtains

$$\frac{\partial \Phi^{t(k)}_{n+1}}{\partial \sigma} = \pm \left[\Delta\alpha(T_{n+1} - T_0) + \Delta S : \sigma^{(k)}_{n+1} + \Lambda^{t(k)}_{n+1}\right] \tag{54}$$

$$\frac{\partial \Phi^{t(k)}_{n+1}}{\partial \xi} = \pm \left[\frac{\partial\beta^{(k)}_{n+1}}{\partial \xi} : \Lambda^{t(k)}_{n+1} + \frac{\partial\eta^{(k)}_{n+1}}{\partial \xi}\right] \tag{55}$$

The cutting plane return mapping algorithm for the SMA constitutive model under the adiabatic/isothermal conditions and considering the TRIP effect is presented in Table 2.

2.4. The XFEM formulation

In this paper, the XFEM is utilized for modeling the fiber bridging phenomenon in fracture analysis of unidirectional composites reinforced with the SMA wires. One of the main advantages of the XFEM is consideration of additional degrees of freedom in the so-called enriched nodes which provide a more realistic approximation compared with the classical FEMs. The displacement, strain and stress jumps along the crack length and the singular behavior around the crack tip could be properly simulated by considering additional degrees of freedom. In addition to improving the discontinuity and singularity approximations, enrichment also reduces the computation cost due to lack of need to very fine elements around the crack tip. The other advantage of the XFEM is that it does not require re-meshing process during crack propagation. In this study we take the first advantage of XFEM because crack growth is not considered here. In this method, several degrees of freedom (DOFs) associated with the discontinuity region are added to the classical finite element DOFs of nearby nodes to provide a higher level of accuracy. The displacement field for a two-dimensional body based on the XFEM assumption is given by Ref. [41]:

$$u^h(x) = \sum_{j=1}^{n} N_j(x)u_j + \sum_{h=1}^{m} N_h(x)(H(\xi^s(x)) - H(\xi^s(x_h)))a_h$$
$$+ \sum_{k=1}^{mt} N_k(x)\left(\sum_{l=1}^{mf} F_l(x)b^l_k\right) \tag{56}$$

where u_j are the nodal displacements (standard degrees of freedom), N_j are the finite element shape functions, ξ^s is the signed distance function, b^l_k and a_h are the additional nodal degrees of freedom for modeling crack tip and crack faces, respectively, n is the sets of all finite element nodes, m is the set of nodes having the crack face in their support domain and

mt is the sets of nodes having the crack tips in their support domain. $F_l(x)$ and $H(x)$ represent the crack tip and the crack faces enrichment functions, respectively which are defined as [42,43]

$$H(\xi^s) = \left\{\begin{array}{l} 1 \forall \xi^s > 0 \\ -1 \forall \xi^s < 0 \end{array}\right\} \tag{57}$$

$$F_l(r, \theta) = \left\{\sqrt{r}\sin\frac{\theta}{2}, \sqrt{r}\cos\frac{\theta}{2}, \sqrt{r}\sin\theta\sin\frac{\theta}{2}, \sqrt{r}\sin\theta\cos\frac{\theta}{2}\right\} \tag{58}$$

After constructing the elemental stiffness matrices and force vectors based on the XFEM formulation and assembling them into the global ones, the discrete system of equations is finally written as [41].

$$ku^h = f \tag{59}$$

in which k is the global stiffness matrix, u^h is the vector of nodal DOF (including both enriched and classical DOFs) and f is the global external force vector. In this study, the effect of bridging fibers is applied by point forces applied to the crack faces. Thus, the components of elemental force vector, f^e_i, are determined as

$$f^e_i = \left\{f^u_i \quad f^a_i \quad f^{b1}_i \quad f^{b2}_i \quad f^{b3}_i \quad f^{b4}_i\right\}^T \tag{60}$$

$$f^u_i = \int_{\Gamma_t} N_i f^t d\Gamma + \int_{\Omega^e} N_i f^b d\Omega + \{P_i\} \tag{61}$$

$$f^a_i = \int_{\Gamma_t} N_i H f^t d\Gamma + \int_{\Omega^e} N_i H f^b d\Omega \tag{62}$$

$$f^{b\alpha}_i = \int_{\Gamma_t} N_i F_\alpha f^t d\Gamma + \int_{\Omega^e} N_i F_\alpha f^b d\Omega \quad (\alpha = 1, 2, 3 \text{ and } 4) \tag{63}$$

f^b and f^t are the external body force and traction vectors, respectively and P_i refers to the concentrated point forces of bridging fibers on the crack edges. These forces, which are determined from the Lagoudas constitutive model, appear in the XFEM formulation after performing the convergence process. $f^{b\alpha}_i$ and f^a_i are the force vector components related to the crack tip and crack faces enrichment functions.

3. Numerical simulation

In this study, the effect of SMA fibers in the discontinuity region is directly applied in the form of point forces. The TRIP effect is also applied in the discontinuity region but ignored in others. The results are obtained in both isothermal and adiabatic conditions. A standard four-node rectangular element is used for discretizing the two-dimensional bodies, and the fracture behavior in the specimen is simulated quasi-statically by XFEM in several time steps. At each time step, the changes include the external force exerted on the specimen as well as the forces generated by the bridging fibers on the crack edges. At each time step, the values of point forces generated by the bridging fibers are obtained in an iterative procedure and after convergence of the
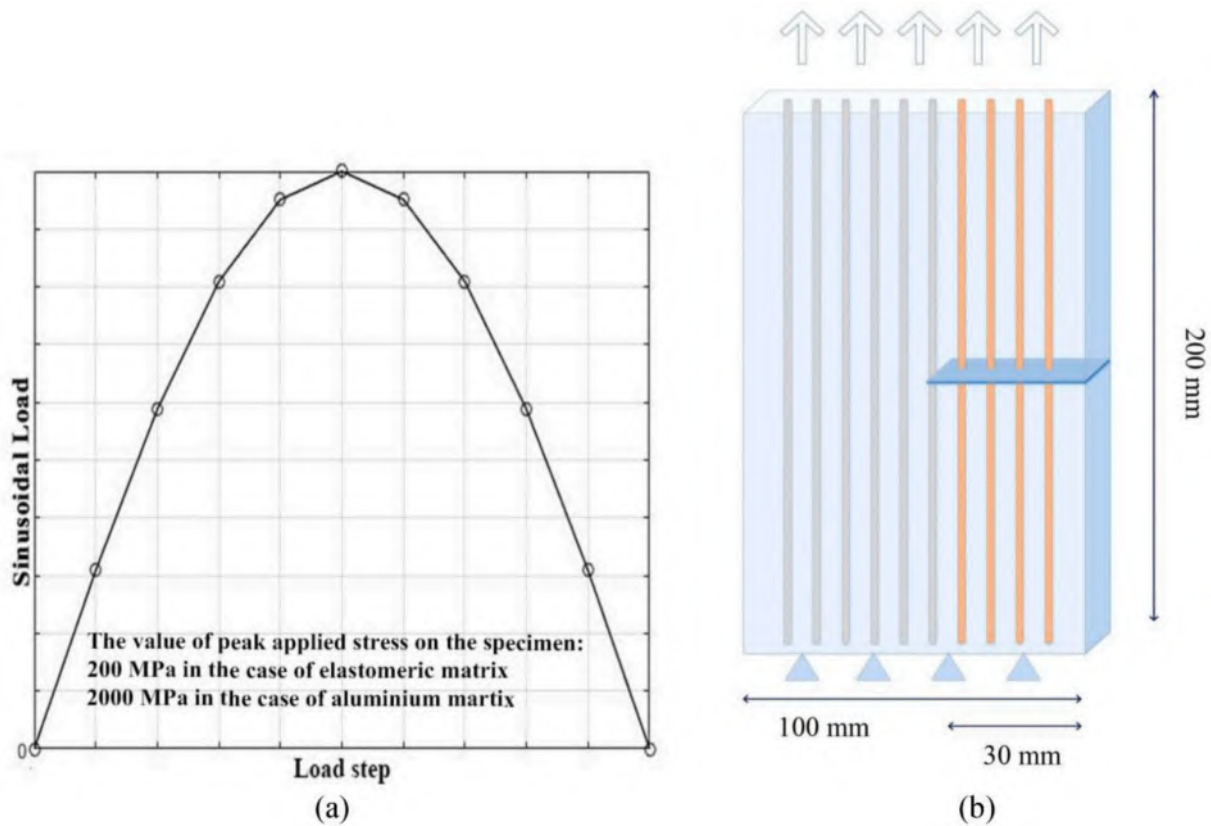
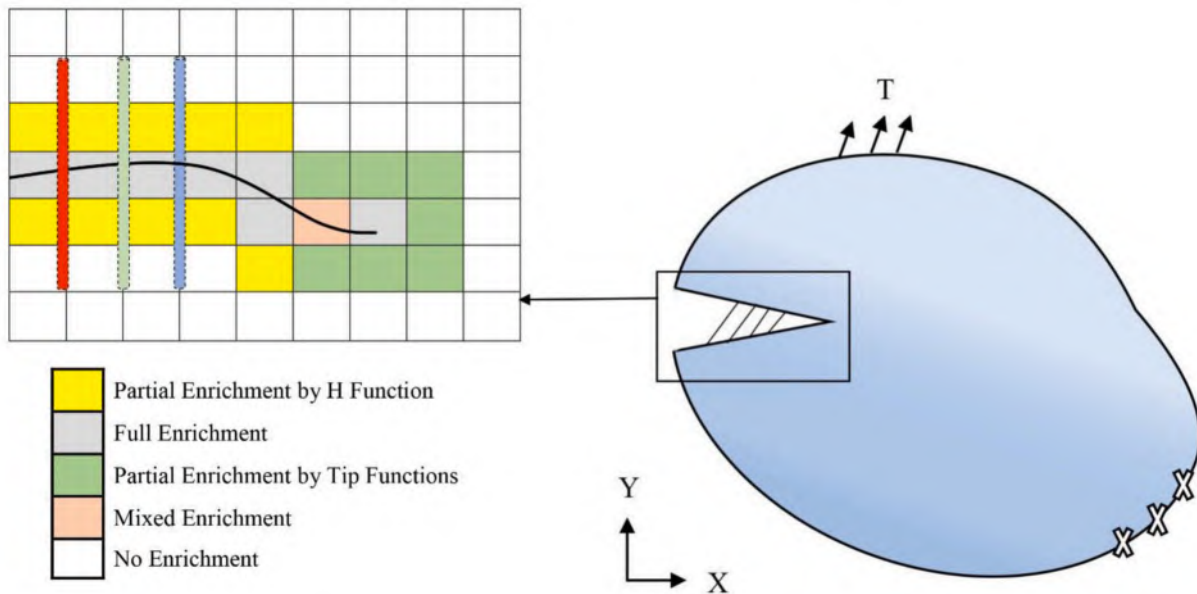**Fig. 2.** (a) Schematic presentation of the sinusoidal load; (b) Schematic view of the composite specimen.

Fig. 3. Direct numerical modeling of SMA fibers with a schematic view of the fiber bridging and the local debonding length, within the XFEM mesh.

displacements. In this paper, crack length is kept constant, and crack propagation is ignored. A view of the composite specimen, its dimensions, crack position, fibers directions, and type of loading, are illustrated in Fig. (2). The analysis is performed in the plane strain state using the force-control loading condition. Figure (3) shows the schematic view of fiber bridging and the effective length of the bridging fibers in the crack area, within the XFEM mesh.

Figure (4) shows how to find the value of residual stress due to the

TRIP strains in the bridging fibers as a sample. At the end of the loading cycle, the external load applied to the specimen reaches zero, but as observed, the residual strains of the SMA fibers produce some residual stress. It should be mentioned that by considering the TRIP effect in the individual SMA fibers the initial stress-strain state (red dot) is obtained, but by taking into account the interaction between the fibers and the composite matrix and after performing the converged iterative process the final conditions (green dot) are determined.
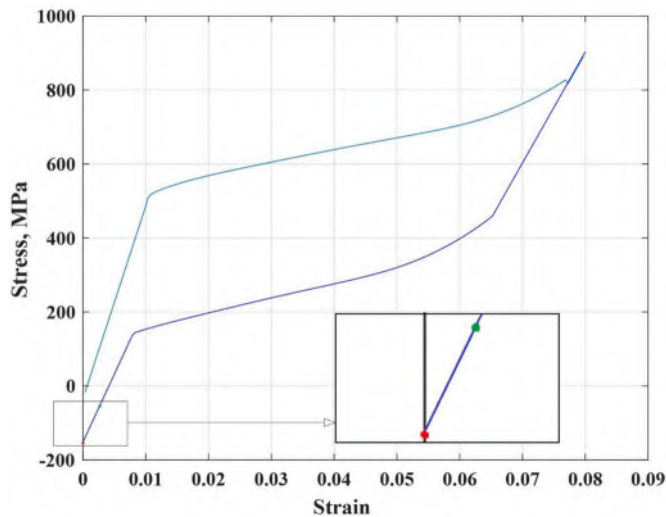
Fig. 4. Residual strains of SMA bridging fibers in the composite specimen used in the XFEM analysis (A sample for understanding how to find the residual stress).
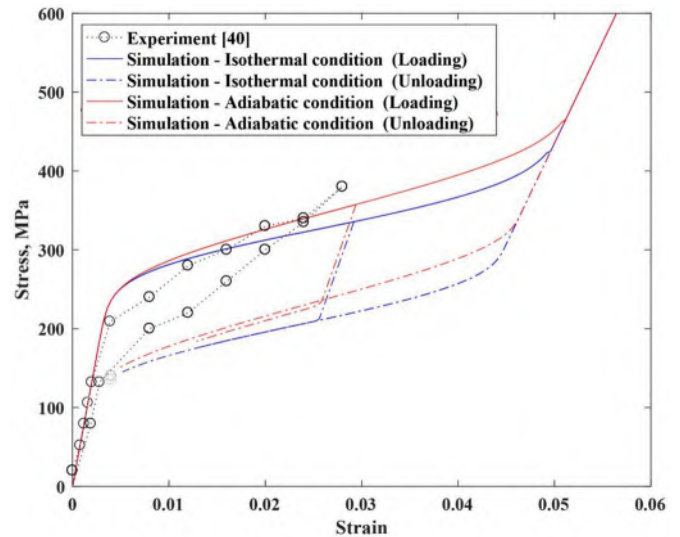

Fig. 6. Comparison of numerical and experimental pseudoelastic stress versus strain considering different thermal conditions without TRIP.

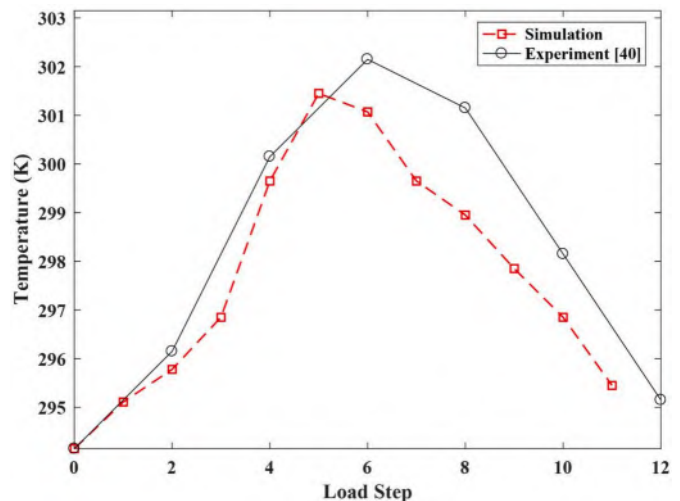**Fig. 5.** Comparison of current TRIP numerical model and experimental pseudoelastic stress-strain results.

Fig. 7. Comparison of the temperature changes during the loading cycle predicted by the simulation and the experimental test data.

In the next step, the obtained values of stress, strain, temperature, and residual strain in the monolithic SMA wire are validated. The thermomechanical behavior of the monolithic SMA is then investigated in more detail. Finally, by considering the effect of bridging fibers, the fracture parameters of the composite specimen with through-thickness cracks are extracted. Also, the effect of mechanical properties of the matrix, the volume fraction of the fibers, and the temperature conditions are investigated.

3.1. Monolithic SMA

In the present study, the formulation required to use the Convex Cutting Plane optimization model, which is a mathematical method for achieving a simpler algorithm, is extracted for the first time in the cyclic loading of SMAs considering the TRIP effect. Thus, in the first step, the adopted formulation and corresponding results should be verified. An SMA wire with the thermomechanical characteristics presented in Table 1 is considered under the axial loading and unloading cycle. The stress-strain curve obtained from the numerical method is compared with the results of laboratory work [39] in Fig. 5. The loading is

considered at an initial temperature of 343K and a stress limit of 900 MPa. At this stage, the temperature is assumed to be constant. What can be inferred from Fig. 5 is the proper accuracy of the simulation results compared to the experimental ones. The accuracy of the simulation is more evident in the transformation-induced residual strain at the end of the loading and unloading cycle. Fig. 5 reveals that the loading is in full transformation mode.

Another issue addressed in this paper is the extraction of the equations for temperature changes due to exothermic and endothermic phase transformation processes during the loading and unloading of nitinol alloy considering the TRIP effect. To check the precision of the work, the simulated model in the case of thermomechanical coupling is compared with the experimental results [40] in cyclic loadings applied on the wire (50.8 at.% Ni) in the adiabatic conditions at temperatures higher than the austenitic finish temperature. Fig. 6 compares the stress-strain values in isothermal and adiabatic conditions with the experimental results. As shown in this figure, temperature changes of the alloy during the loading and unloading lead to a shift to higher stress values. The reason for the partial mismatch in the experimental and simulation models in Fig. 6 could be attributed to the dependence of the material
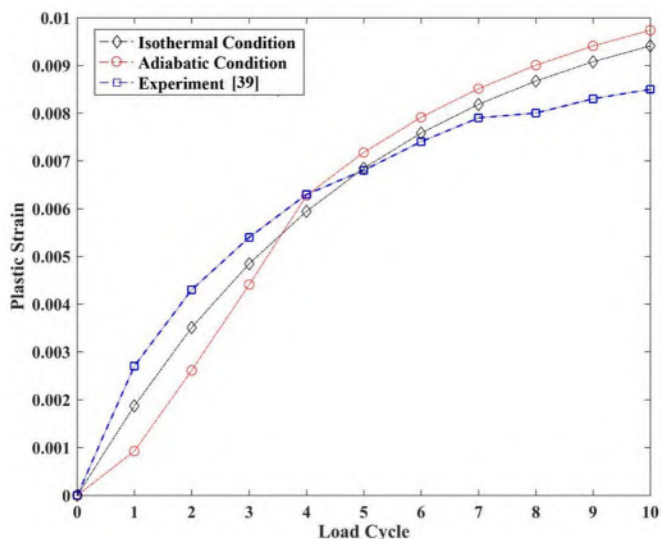
Fig. 8. Comparison of the residual strain accumulated during the cyclic loadings (up to a constant maximum value of stress) predicted by the simulation and the experimental test data.
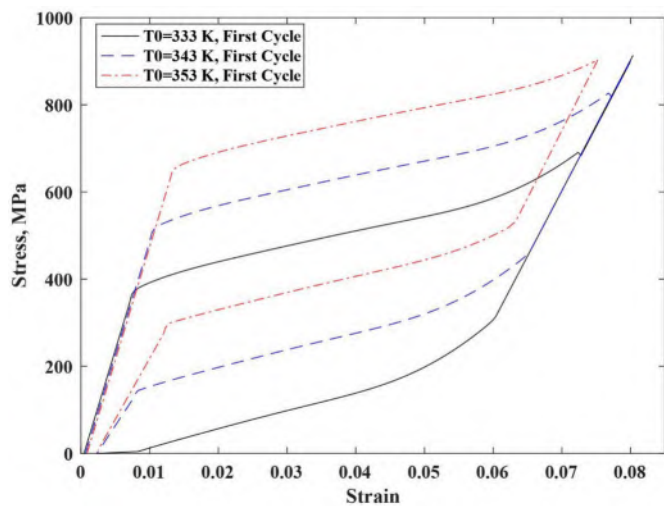

Fig. 9. Stress-strain response of NiTi SMA to the first load cycle (up to a constant value of stress) considering various initial temperatures.

Fig. 10. Temperature-strain response of NiTi SMA to the first load cycle (up to a constant value of stress) considering various initial temperatures.

Fig. 11. Temperature changes during the first 10 cycles of loading (up to a constant value of stress) considering various initial temperatures.

parameter Y on another parameter called γ, which is not included in the formulation of this research [6,7]. The material parameter Y is related to the total area enclosed by the hysteresis curve during a complete phase transformation. The effect of parameter γ is on the minor loop curvature. The minor loops occur due to incomplete forward phase transformation. Fig. 7 shows that in the loading path, a temperature increase of about 9K is observed in the experimental study [40], which is in good agreement with the temperature increase of 8.3K in the simulation model. At the end of the loading-unloading cycle, a temperature increase of about 1K remains in the alloy.

The rate of plastic strains reaching saturation for alloys with mechanical properties defined in Table 1 under the cyclic loading in both the isothermal and the adiabatic conditions are compared with the results of the experimental work [39] in Fig. 8. As observed, the obtained results are validated with good accuracy.

At this stage, the effects of the initial temperature on the thermo-mechanical response of the first pseudoelasticity load cycle with the TRIP effect are investigated. Fig. 9 shows that the temperature increase leads to a reduced percentage of the phase transformation, although
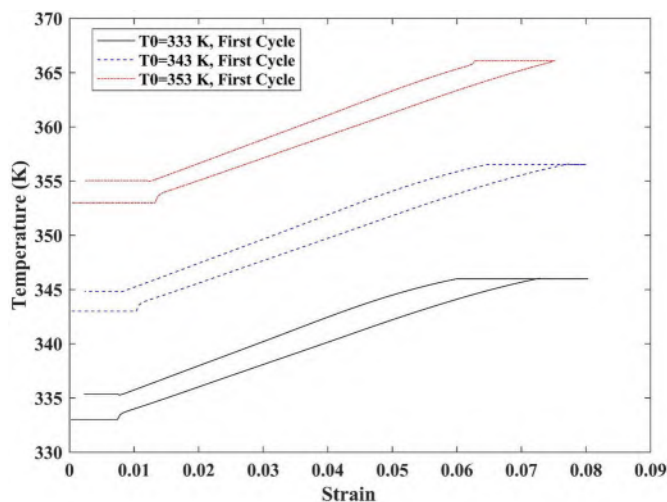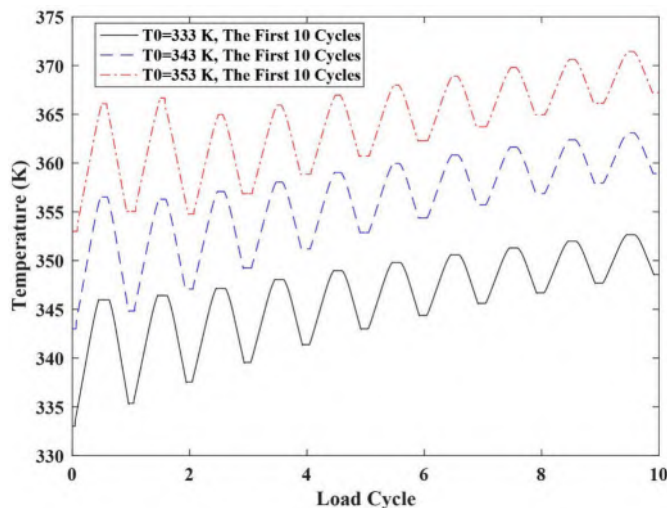
with a shift in a positive direction along the vertical axis. The reduction in the phase transformation means that at higher temperatures, the SMA wire reaches the 900 MPa stress level sooner and does not allow for the generation of the fully martensitic states. This is well observed in the 353K cycle.

Moreover, the effect of initial temperature on the amount of plastic strain in one cycle is shown in Fig. 10. It can be seen that at higher temperatures, the value of plastic strain increases (if the temperatures are higher than the austenitic finish temperature). However, the alloy behaves reversely at lower temperatures [4]. The present study aims to examine pseudoelasticity loadings; thus, the desired temperatures are higher than the austenitic finish temperature. So, the amount of TRIP strain has an upward trend with the increase in the initial temperature, albeit slightly.

Another issue presented in Fig. 10 is the temperature change in each loading-unloading cycle. The results showed that at higher initial temperatures, the internal temperature increase caused by the adiabatic condition declines at the end of each cycle. At the end of the loading cycle at 333K, the specimen temperature increases by 2.4K compared to the initial state. The temperature increase is 1.8K in the cycles with higher initial temperatures; a reason for that could be the change from
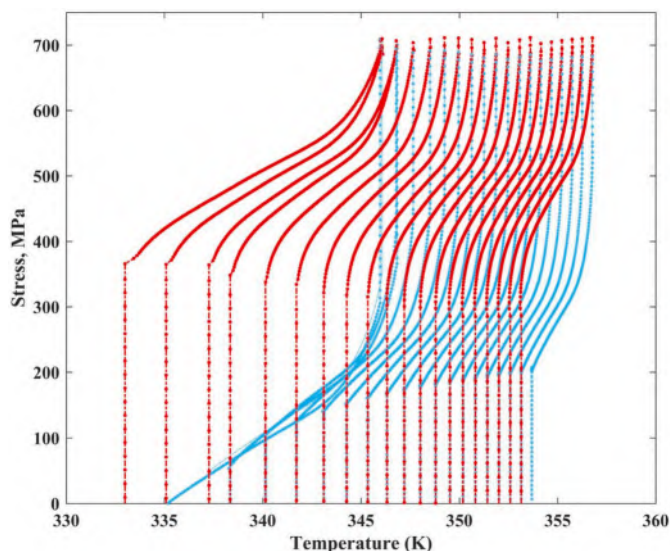
Fig. 12. Stress-temperature response of NiTi specimen to cyclic loading (up to a constant value of stress) under the adiabatic condition.

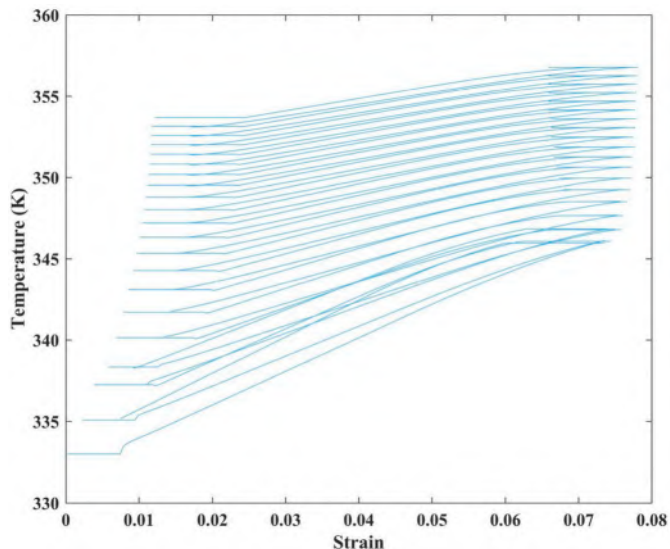**Fig. 13.** Strain versus temperature response of NiTi specimen to cyclic loading (up to a constant value of stress) under the adiabatic condition.

Fig. 14. Cyclic stress-strain-temperature response to a constant value of stress under the adiabatic condition.

Fig. 15. Cyclic stress response: the isothermal and the adiabatic conditions.

the major transformation loop to the minor one in each cycle because the martensitic transformation process would become more incomplete with the initial temperature increase under the constant load. The same is true, albeit to a lower extent, about periodic loadings as shown in Fig. 11.

The SMA specimen is then subjected to cyclic loadings with a constant stress limit of 700 MPa at an initial temperature of 333 K. The thermomechanical behaviors for twenty initial loading cycles are shown in Figs. 12–16. The constant stress limit of 700 MPa is selected so that in the studied twenty cycles, the reciprocal transformation takes place completely; Therefore, saturation in the production of martensitic TRIP strain would be reached in a smaller number of cycles. The comparison of the stress-strain-temperature responses shows that the stress level of the twentieth cycle is significantly lower than that of the first. In addition, the dissipative energy decreases during the cyclic loadings and unloadings and could be calculated using the area enclosed within the hysteresis loops.

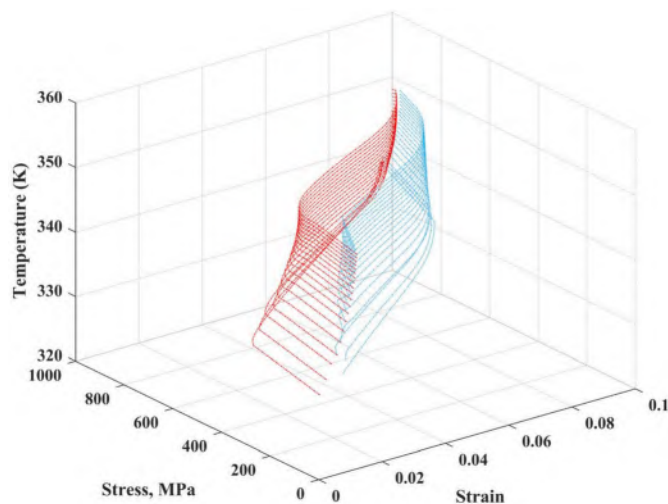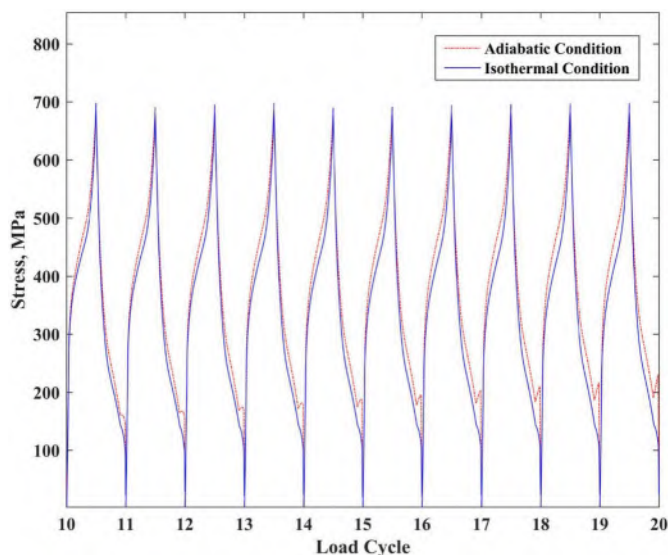Fig. 12 presents the stress-temperature graph for the cyclic loading.

The temperature increase in the specimen can be seen in each cycle, and this temperature difference decreases with an increase in the number of loading cycles. The first loading cycle starts with an initial temperature of 333 K, and finally, the temperature increases by about 20K after the twenty cycles. As can be observed, smaller temperature changes occur in the end cycles; caused by the smaller changes in the stress and strain due to the reduced area enclosed between the reciprocal paths in the stress-strain graph, namely the dissipation.

Fig. 13 well indicates the beginning of the plastic strain until reaching saturation. Complete phase transformations occur in all loading-unloading cycles. In other words, the alloy is first in the full austenite region in all stages, and after loading, the martensitic volume fraction reaches the unity value. Finally, it reaches from the full martensitic phase to the full austenite phase. According to Fig. 13, at the peak of each loading cycle, the curve lines are converted to straight lines, indicating that the material moves a distance, albeit a small one, towards the complete martensite area. For better illustration, three-dimensional diagrams are depicted in Fig. 14.

As shown in Fig. 15, when the temperature increase due to the exothermic transformation from austenite to martensite and the
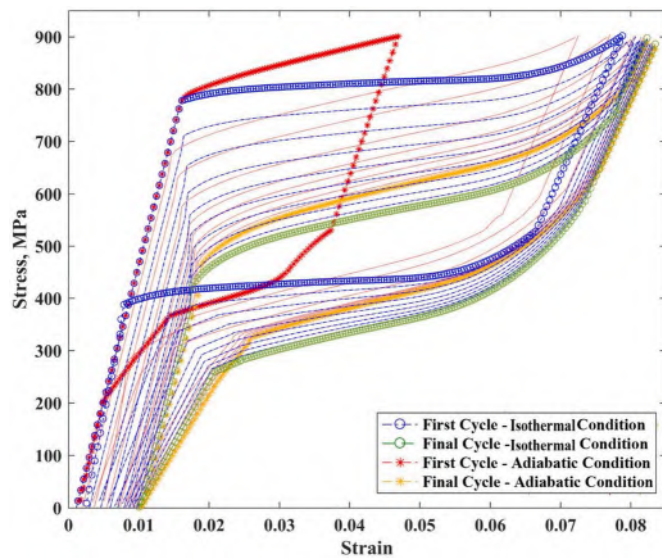
Fig. 16. Cyclic stress versus strain plots: the isothermal and the adiabatic conditions.

endothermic transformation from the martensite to the austenite increases the stress level, the condition becomes closer to the adiabatic condition at high-rate loadings where there is not enough opportunity to transfer heat from the alloy to the environment or the matrix.

Fig. 16 compares the isothermal and adiabatic conditions concerning the TRIP. The SMA with the mechanical properties of Table 1 is considered at an initial temperature of 363 K under stress control. It is clear that the temperature increase due to the adiabatic conditions intensifies the stress level, while the peak stress is considered as a loading limit of 900 MPa. In this type of cyclic loading, the conversion of the condition from the isothermal to the adiabatic one causes the full transformation cycles to change to partial ones. The response of the SMA for the cyclic loading, up to a constant value of stress, shows that the transformation response after 10 loading cycles has been saturated and it also shows the downward trend in terms of generating plastic strains. The SMA evolution has revealed by passing loading cycles and the stress value in the last loading cycle is lower than the first cycle. Contrary to what happens to stress field, the transformation hardening during the loading cycles experiences upward trend. Also, the area enclosed by the transformation hysteresis loop for the last cycle is smaller than the area enclosed by the initial loop.

3.2. SMA/elastomer composite material and SMA/aluminium composite material

This section deals with the fracture behavior of a composite specimen with nitinol-reinforcing fibers. Two types of matrices, i.e. elastomeric and aluminium, with lower and higher elasticity modulus than SMA fibers, are selected. Their mechanical properties are shown in Tables 3 and 4.

Basically, slippage between fibers and matrix affects the thermomechanical response of the composites. The occurrence of interfacial slip can decrease the structural stiffness and increase the deflection, and consequently reduce the elastic flexural capacity of the composites. Also the structural performance degradation or potential damage induced by the slippage may lead to the global failure of the structure. In reality,

Table 3
Material properties of the epoxy polymeric matrix [19].

Elastic parameters of the isotropic epoxy polymeric matrix.	$E =$ 3.45 GPa	$\nu =$ 0.35	$\rho c = 1.28$ MJ/ (m^3K)

Table 4
Material properties of the aluminium matrix [19].

Elastic parameters of the isotropic aluminium matrix.	$E =$ 72.4 GPa	$\nu =$ 0.33	$\rho c = 2.25$ MJ/ (m^3K)

shear connections are having deformability with a finite stiffness, which results in the development of interfacial shear slip [44, 45]. There are several approaches to take into account the interfacial slippage such as modeling fibers by appropriate element in finite element method or utilizing simplified techniques for considering the effect of slippage along the length of the fiber. However, in many studies, the bond between fiber and matrix is considered ideal [15,16,21,34] and in this article also, the effect of slippage is ignored.

The behavior of an individual SMA fiber (Unconstrained fiber) and an SMA fiber bonded within the matrix (Constrained fiber) is quite different. The analytical and experimental studies on SMA wire-reinforced composites show that due to the difference between the shear modulus of matrix and SMA wire, and because of the strain non-uniformity at the SMA wire-matrix interface, shear stress is developed within the matrix under the axial loading of the volume element. The interface effect could change the SMA wire stiffness in the context of SMA composites. Also, the stresses required for inducing the phase transformations for a constrained SMA wire is higher than an unconstrained SMA wire [46].

In this research, the effects of fibers in the crack area have been considered in the form of several point forces applied to the crack boundaries. The connection between the fiber and the matrix is considered ideal and no slippage occurs between them. The axial stress distribution is applied in nitinol fibers along the length of the wire, and for this purpose, the direction of force applied in the bridging fibers is calculated at each step. Since the induced load by each constrained fiber is different from an individual fiber, the force values of SMA fibers at each load step is determined in a convergence loop. Firstly, without considering the fiber bridging effect the problem is solved and the crack opening displacement and consequently the strain applied to each fiber is determined. Then according to the fibers strain, the amount of stresses and consequently forces of individual (unconstrained) wires are calculated. After that, by applying the point forces of fibers to the crack boundaries, the whole structure is again solved and the strains of fibers is calculated. This process is repeated until the difference of fibers strains in two subsequent iteration will be lower than a defined tolerance. Actually, the interaction between fibers and composite structure is considered by this approach, and the convergence process has guaranteed the correct amount of force applied in the structure. Table 5 illustrates the flowchart of convergence algorithm for determination of fibers force.

A sinusoidal applied load is considered on the composite specimen. In this part, the matrix is considered isotropic. The relationship between the volume fraction of shape memory fibers and the number of fibers bridging on the crack edges is given in Table 6. The values of peak applied stress for the composite specimen with a unit width and the crack length of 0.03 m are considered 200 MPa in the case of the elastomeric matrix, and 2000 MPa in the case of the aluminium matrix. The initial temperature of the nitinol fibers is set to 343 K, and the specimen behavior is examined in both adiabatic and isothermal modes. The results of the elastomeric and aluminium matrix composites are presented, respectively. Table 7 shows a good agreement between the numerical and analytical methods [42] for calculating the stress intensity factor (SIF) for different stresses applied to the two-dimensional specimen. In this case, no bridging fiber is considered on the crack region.

Fig. 17 indicates the changes of first mode SIF in the elastomeric composite specimen reinforced with SMA fibers in a loading cycle. According to the results, the increased volume fraction in the composite specimen causes the SIF to decrease further. As the load on the specimen increases, the shape memory fibers are gradually transformed from the

Table 5
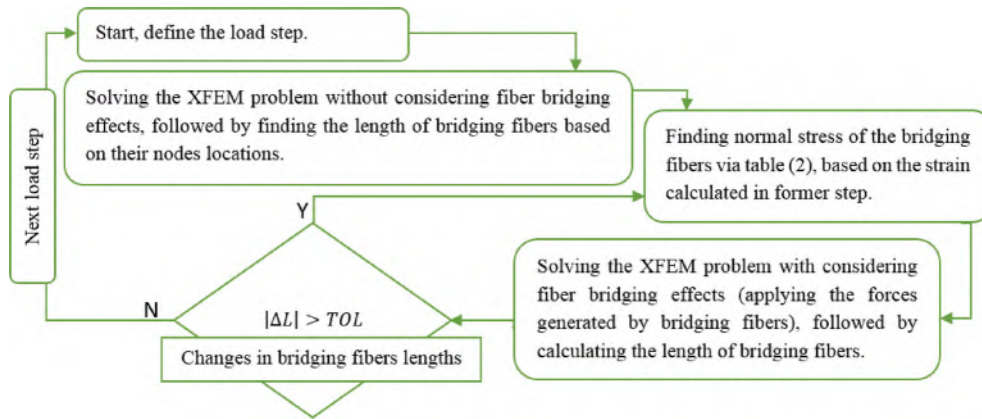Flowchart of convergence algorithm for determination of fibers force.

Table 6
Composites parameters.

Fiber volume fractions of the composite specimen.	3 %	5 %	10 %
Number of bridging fibers	3	4	8

Table 7
Percentage error of SIF for different applied stress on the two dimensional specimen.

Stress, MPa		200	180
Mode I *SIF*, MPa$\sqrt{\text{m}}$	Numerical method	10.29	9.29
	Analytical method	10.19	8.92
	Percentage of error	1 %	3.7 %
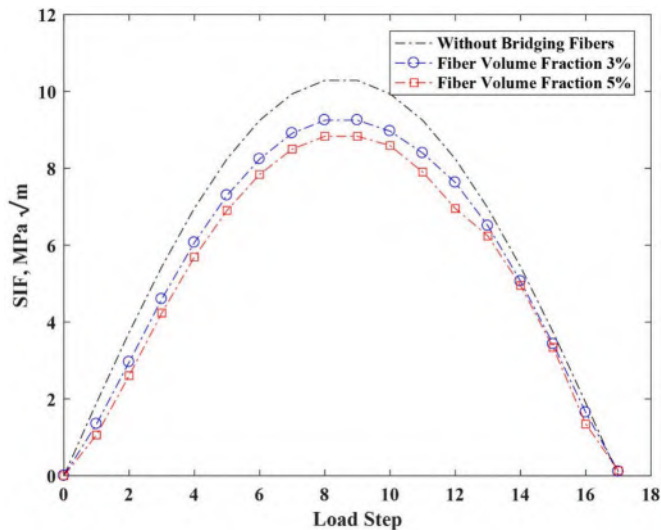
Fig. 17. SIF versus loading steps for the SMA/elastomer composite specimen with different fiber volume fraction values (adiabatic condition with TRIP).

Fig. 18. Normal stress in the loading direction as a function of distance from the crack tip for the SMA/elastomer composite specimen in the ninth loading step (adiabatic condition with TRIP).

austenitic to the martensitic phase, with a higher induced stress level than the return path of transformation from the martensitic to the austenite phase. The difference in the stress levels at the reciprocating path of the fiber pseudoelasticity loading cycle is well observed in Fig. 17. The number of bridging fibers on the crack region at the volume fraction of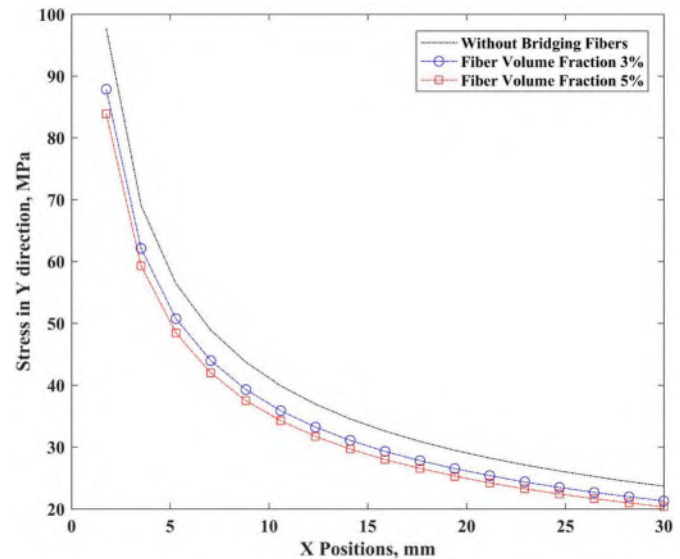 3% and 5% is 3 and 4, respectively. Examining the forces produced by the opening of the crack edges shows that in the case of 3 bridging nitinol fibers, only the fiber that is farthest away from the crack tip undergoes a complete phase transformation. The two remaining bridging fibers begin to pass the return path before the full martensitic phase transformation and go back to the full austenite phase. When the number of bridging fibers at the crack edges is four, none of them experience full martensitic transformation in the pseudoelasticity process, and all begin the return path in the incomplete martensitic region. This could be due to the increase in the level of the applied traction on the crack edges. In the other words, the fibers like some inhibitors reduce the crack opening displacement and, ultimately, prevent the complete phase transformation.

Fig. 18 shows the diagram of normal stress in the direction of the applied force (σ_Y) versus horizontal distance from the crack tip (X) in the elastomeric composite with nitinol fibers. The illustrated stresses correspond to the ninth step of the sinusoidal loading cycle with peak stress of 200 MPa. As observed, the increase in the volume fraction of the fibers reduces the stress values. As expected, the stress level also decreases by going away from the crack tip.

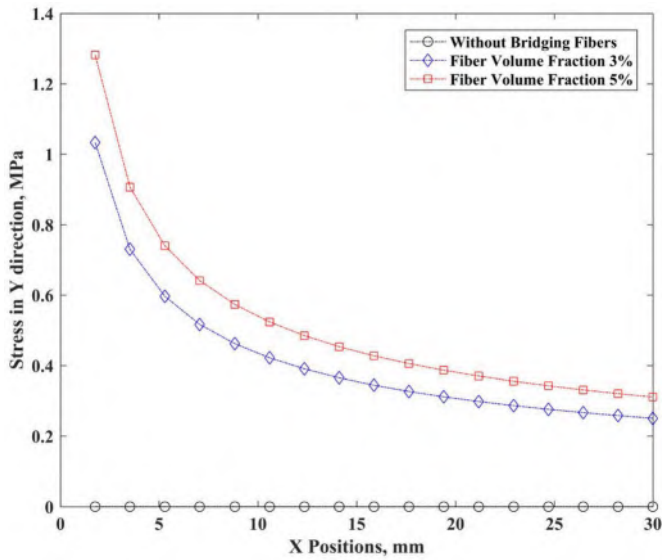In Fig. 19, considering different fiber volume fractions, the residual

Fig. 19. Residual stress in the loading direction as a function of distance from the crack tip for the SMA/elastomer composite specimen at the end of loading cycle (adiabatic condition with TRIP).
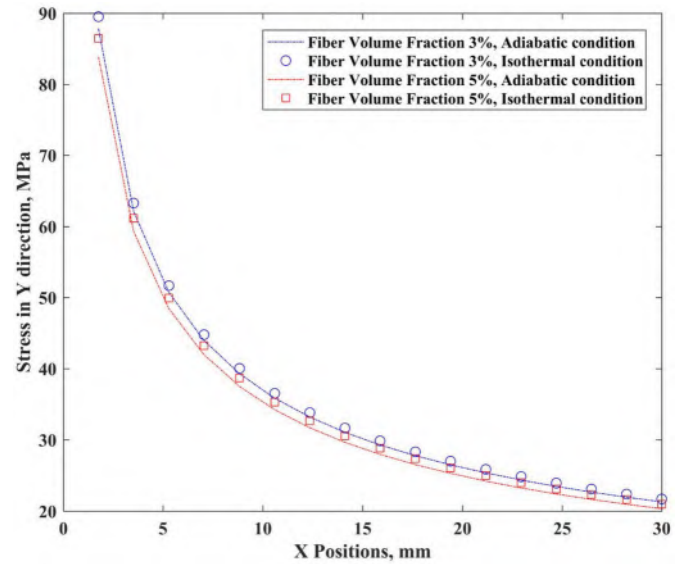

Fig. 21. Normal stress in the loading direction as a function of distance from the crack tip for the SMA/elastomer composite specimen in the ninth loading step considering the adiabatic and the isothermal conditions.
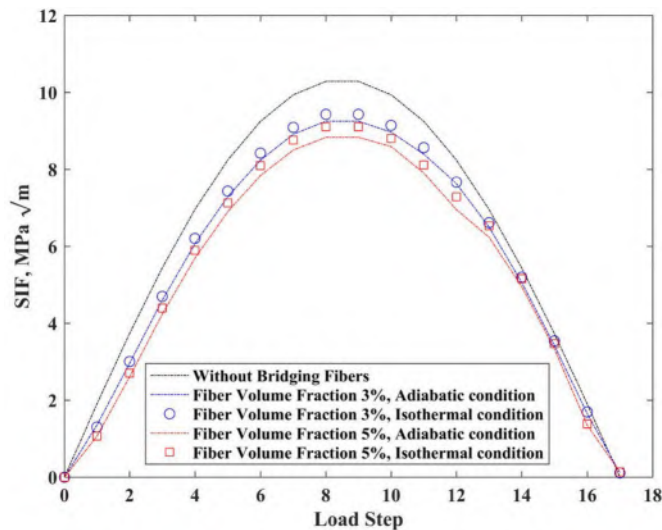

Fig. 20. SIF versus loading steps for the SMA/elastomer composite specimen considering the adiabatic and the isothermal conditions.
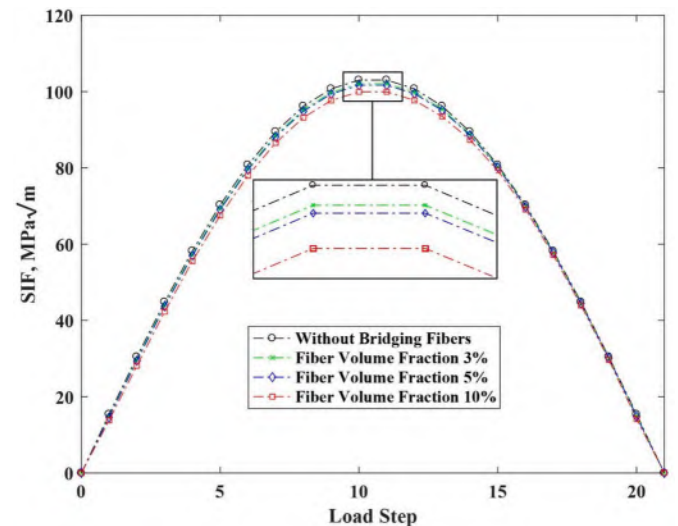

Fig. 22. SIF versus load step for the SMA/Aluminium composite specimen considering different values of fiber volume fractions (adiabatic condition with TRIP).

stress values resulting from the irreversible strains in the nitinol fibers are compared during the phase transformation. This figure shows the change of residual stress with respect to the applied force with the change in the volume fraction of the fibers. At the final step, the external force on the specimen reaches zero, but the plastic strains of SMA wires cause some residual stress. In the absence of bridging fibers, no residual stress would be obtained. However, as the number of bridging fibers increased, the residual stress along the crack tip in the first loading mode increased as well. The remarkable point is that increasing the number of bridging fibers does not necessarily increase the residual strain; only the fibers that undergo the phase transformation affect this type of stress. In the elastomeric specimen, all the fibers enter the martensitic phase from the initial austenitic phase. However, only one fiber experiences the complete phase transformation when the volume fraction of the fibers is 3%.

In Figs. 20 and 21, the fracture behavior of the SMA/elastomer composite specimen is investigated for adiabatic and isothermal

conditions by considering the TRIP effect. The SIF values for the adiabatic condition are lower than the isothermal condition; which is related to the increased stress level in the stress-strain diagram of SMA in the adiabatic condition compared to the isothermal one. The adiabatic condition is generally applied for high loading rates. In the specimen with a higher volume fraction, the SIF has a greater decrease as well.

Figs. 22–24 show the effect of the bridging fibers on the fracture behavior of the SMA/Aluminium composite specimen. In these figures, considering different fiber volume fractions, the effects of the smart fibers on the SIF, the normal stress in *Y* direction in the crack tip region, and the residual stress due to fiber plastic strains are investigated. It is assumed that for the fiber volume fractions of 3%, 5%, and 10% respectively, 3, 4, and 8 fibers are bridging across the crack faces and the corresponding point forces are applied on the crack edges. It is observed that for all fiber volume fraction indices, none of the fibers experiences complete martensitic phase transformation in the external stress level of
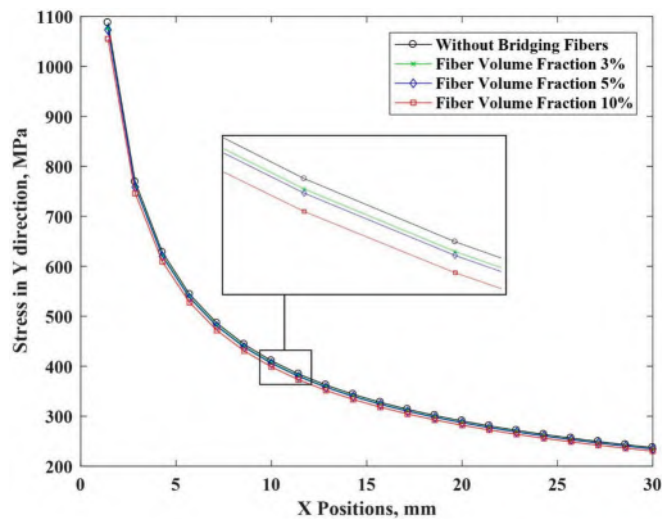
Fig. 23. Normal stress in the loading direction as a function of distance from the crack tip for the SMA/aluminium composite specimen in the eleventh loading step (adiabatic condition with TRIP).
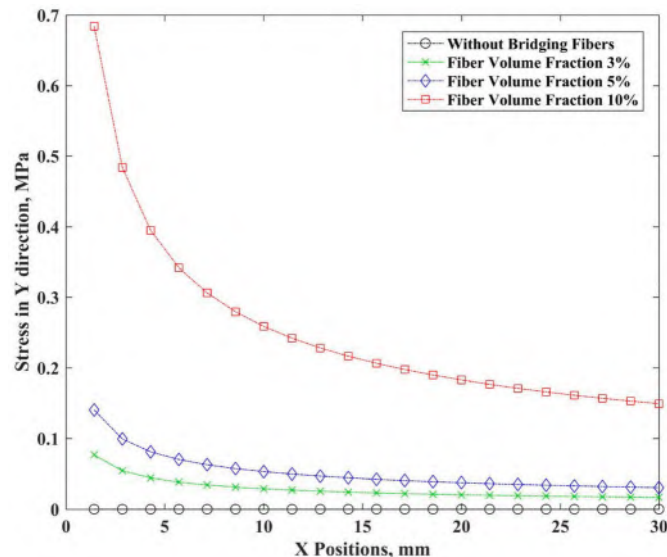

Fig. 24. Residual stress in the loading direction as a function of distance from the crack tip for the SMA/aluminium composite specimen at the end of loading cycle (adiabatic condition with TRIP).

2000 MPa. The bridging fibers improve the behavior of the material against the fracture, and this effect is more evident in the specimen with a higher fiber volume fraction. As observed in Fig. 23, the increased number of bridging fibers reduces the stress level in the specimen at the eleventh step of loading, but as observed in Fig. 24 a greater negative effect is created on the residual stress resulting from the TRIP effect in the final step where the external force on the specimen becomes zero.

Fig. 25 compares the SIF values for the two types of composites with elastomeric and aluminium matrices, considering different volume fractions. The elastomeric- and aluminium -matrix composite are considered under the load cycle with the maximum value of 200 and 2000 MPa, respectively. The SIFs shown in this figure are related to the end of the loading cycle when the specimen is subjected only to the stress caused by the plastic strain of the fibers. The SIF results from the residual strain in the elastomeric matrix specimen have higher values. This is due to the lower stiffness of elastomer compared to aluminium because it causes nitinol fibers to withstand more displacements, and
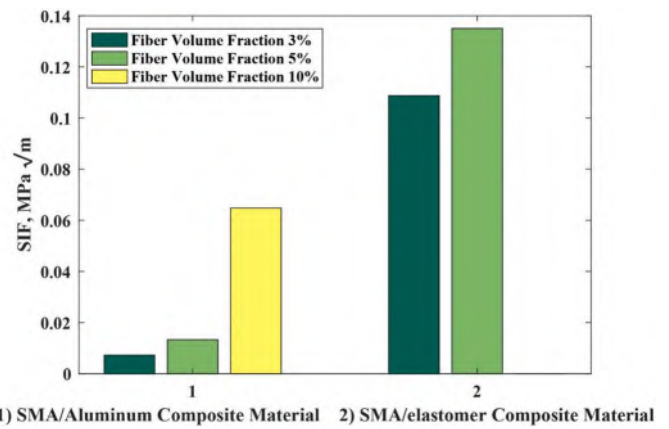

Fig. 25. SIF of the composite specimens at the end of the loading cycle (adiabatic condition with TRIP).

more displacements would lead to higher TRIP strain and, consequently, greater SIF.

The displacement and the stress contours during the loading and at the end of unloading, are depicted in Fig. 26. At the end of unloading (b and d in Fig. 26), the plastic strains of bridging fibers, or so-called transformation induced plasticity, generate some residual stresses in composite structures.

Finally, the fiber size effect, which is an important factor for material design in industrial applications, has been examined. The effect of diameter of SMA wires on the stress intensity factor of the SMA/elastomer and SMA/aluminum composite specimens is investigated in Figs. 27 and 28. As observed, by increasing the diameter of SMA wires, the stress intensity factor decreases which shows the more effective performance of thicker wires in reducing the fracture parameter of the structure.

4. Conclusion

In this research, the fracture response of composite plates reinforced with SMA fibers under pseudoelastic loading has been investigated. To deal with the fiber bridging phenomenon, the thermomechanical coupling of SMA fibers in cyclic loadings by considering TRIP has been addressed. Numerical simulations are compared with the experimental and analytical data, which show a good agreement. In summary, the following results have been observed:

- The response of the monolithic SMA undergoing TRIP shows that lower temperature changes occur in the end cycles before saturation. The reduction percent of the temperature changes is more than 50% for the Ti-49.7 at. %Ni alloy under the adiabatic condition.
- Increasing the initial temperature in each cycle of loading on SMA wire leads to the changes from the major transformation loop to the minor one under a constant maximum load, which affects some parameters such as the plastic strain and the temperature changes.
- The nitinol fibers bridging across the crack contribute to the strength of the composite structure against fracture in a loading cycle. However, it has much greater effects on composites with elastic modulus lower than the nitinol fibers (such as elastomers).
- Although loading bridging of the nitinol fibers during the pseudoelasticity helps to reduce the SIF of cracked composite with elastomeric matrix more than with the aluminium case, the residual stress level of the elastomeric composite is higher than the aluminium case at the end of loading.
- Increasing the number of bridging fibers helps to reduce the SIF. However, it raises the probability of increasing the residual stress in the composite specimen, which depends on the mechanical
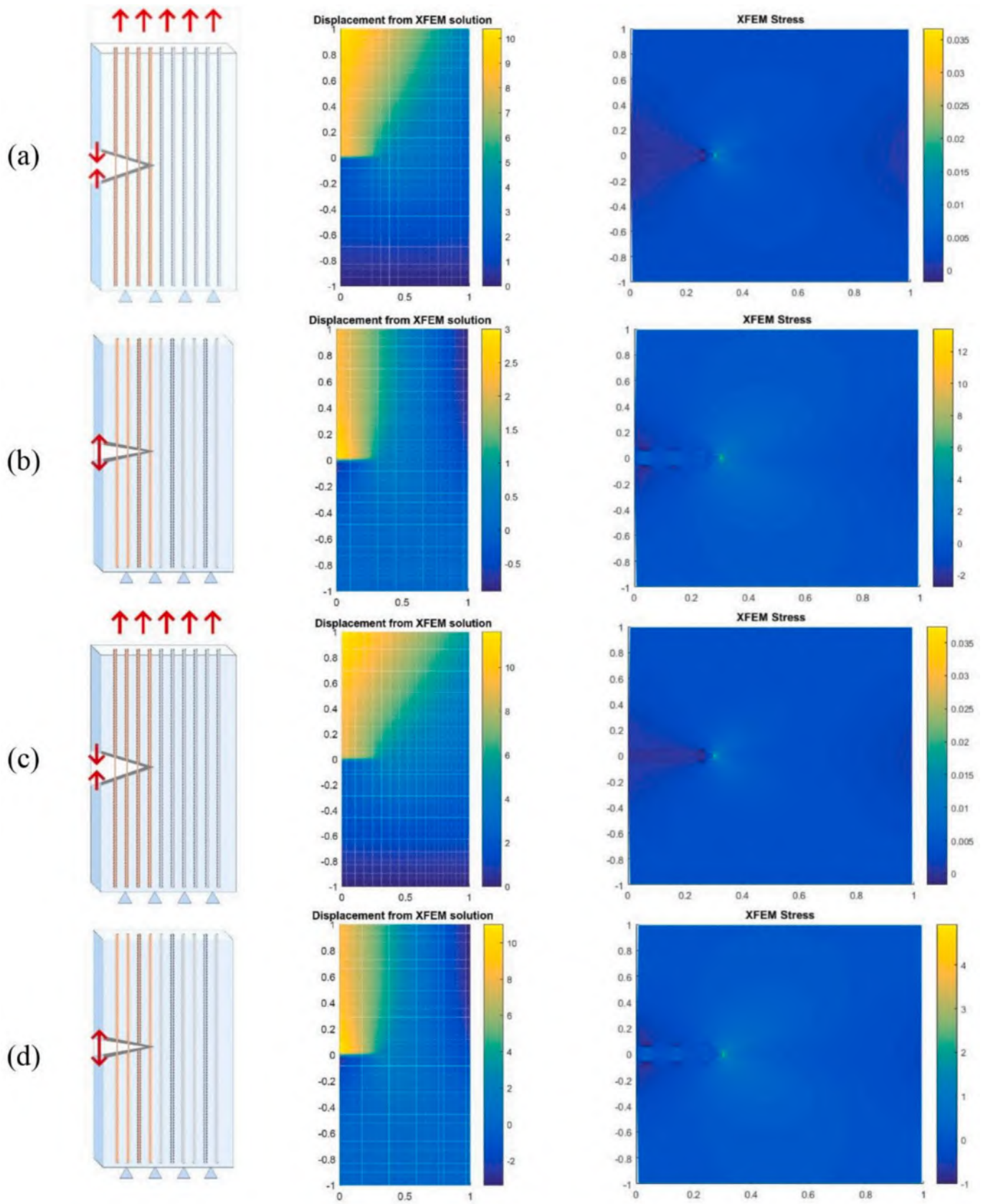
Fig. 26. Displacement and stress contours (a,b) for the SMA/aluminium composite specimen (c,d) for the SMA/elastomer one.
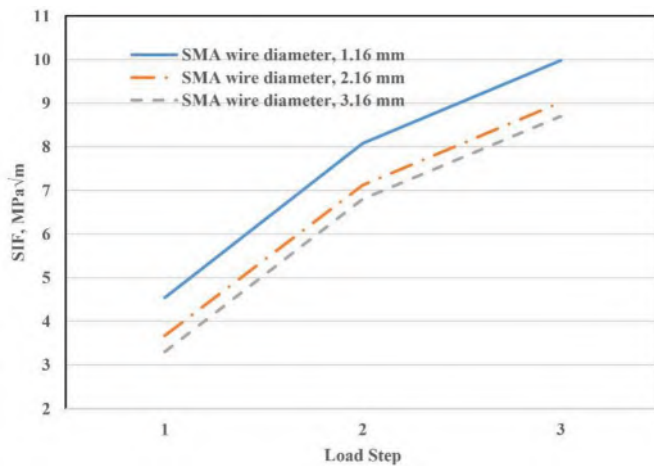
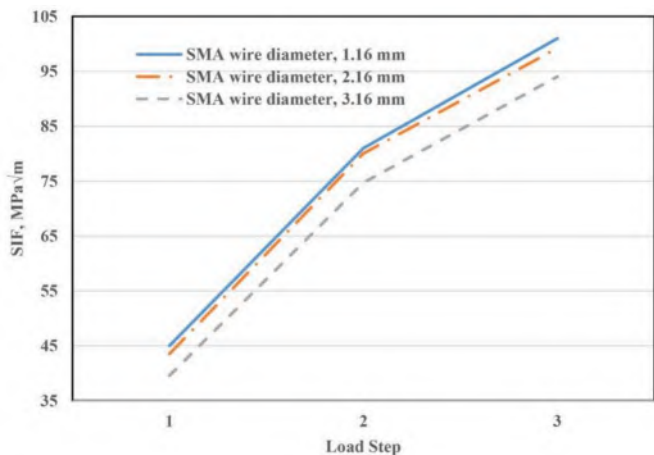**Fig. 27.** Effect of SMA fiber size on the SIF of SMA/elastomer composite specimen (up to 2000 MPa).

Fig. 28. Effect of SMA fiber size on the SIF of SMA/aluminium composite specimen (up to 200 MPa).

properties of the matrix and the amount of the external load applied to the specimen.

- The adiabatic conditions governing the bridging nitinol fibers typically occur at higher-rate loadings, and the results show that compared to the isothermal condition, the adiabatic thermal conditions contribute more to the structural resistance to fracture.

CRediT authorship contribution statement

Amin Ardali: Conceptualization, Methodology, Software, Writing – original draft. **Jafar Rouzegar:** Conceptualization, Methodology, Supervision, Writing – review & editing. **Soheil Mohammadi:** Conceptualization, Methodology, Writing – review & editing. **Mina Karimi:** Methodology, Writing – review & editing.

Declaration of competing interest

The authors declare that they have no known competing financial interests or personal relationships that could have appeared to influence the work reported in this paper.

Data availability

Data will be made available on request.

References

[1] K. Tanaka, A thermomechanical sketch of shape memory effect: one-dimensional tensile behavior, Res. Mech. 18 (1986) 251–263.

[2] J.G. Boyd, D.C. Lagoudas, Thermomechanical response of shape memory composites, J. Intell. Mater. Syst. Struct. 5 (1994) 333–346.

[3] J.G. Boyd, D.C. Lagoudas, A thermodynamical constitutive model for shape memory materials. Part I. The monolithic shape memory alloy, Int. J. Plast. 12 (1996) 805–842.

[4] B. Strnadel, S. Ohashi, H. Ohtsuka, S. Miyazaki, T. Ishihara, Effect of mechanical cycling on the pseudoelasticity characteristics of Ti- Ni and Ti- Ni- Cu alloys, Mater. Sci. Eng., A 203 (1995) 187–196.

[5] C. Liang, C.A. Rogers, One-dimensional thermomechanical constitutive relations for shape memory materials, J. Intell. Mater. Syst. Struct. 8 (1997) 285–302.

[6] Z. Bo, D.C. Lagoudas, Thermomechanical modeling of polycrystalline SMAs under cyclic loading, Part III: evolution of plastic strains and two-way shape memory effect, Int. J. Eng. Sci. 37 (1999) 1175–1203.

[7] Z. Bo, D.C. Lagoudas, Thermomechanical modeling of polycrystalline SMAs under cyclic loading, Part IV: modeling of minor hysteresis loops, Int. J. Eng. Sci. 37 (1999) 1205–1249.

[8] D.C. Lagoudas, P.B. Entchev, Modeling of transformation-induced plasticity and its effect on the behavior of porous shape memory alloys. Part I: constitutive model for fully dense SMAs, Mech. Mater. 36 (2004) 865–892.

[9] P.B. Entchev, D.C. Lagoudas, Modeling of transformation-induced plasticity and its effect on the behavior of porous shape memory alloys. Part II: porous SMA response, Mech. Mater. 36 (2004) 893–913.

[10] S. De la Flor, C. Urbina, F. Ferrando, Effect of mechanical cycling on stabilizing the transformation behaviour of NiTi shape memory alloys, J. Alloys Compd. 469 (2009) 343–349.

[11] H. Yu, M.L. Young, One-dimensional thermomechanical model for high strain rate deformation of austenitic shape memory alloys, J. Alloys Compd. 710 (2017) 858–868.

[12] Y. Chemisky, D.J. Hartl, F. Meraghni, Three-dimensional constitutive model for structural and functional fatigue of shape memory alloy actuators, Int. J. Fatig. 112 (2018) 263–278.

[13] V. Birman, K. Chandrashekhara, S. Sain, An approach to optimization of shape memory alloy hybrid composite plates subjected to low-velocity impact, Composites, Part B 27 (1996) 439–446.

[14] J.H. Roh, J.H. Kim, Adaptability of hybrid smart composite plate under low velocity impact, Composites, Part B 34 (2003) 117–125.

[15] S.M. Khalili, M.B. Dehkordi, E. Carrera, A nonlinear finite element model using a unified formulation for dynamic analysis of multilayer composite plate embedded with SMA wires, Compos. Struct. 106 (2013) 635–645.

[16] S.M. Khalili, A. Shokuhfar, K. Malekzadeh, F.A. Ghasemi, Low-velocity impact response of active thin-walled hybrid composite structures embedded with SMA wires, Thin-Walled Struct. 45 (2007) 799–808.

[17] F. Daghia, D.J. Inman, F. Ubertini, E. Viola, Shape memory alloy hybrid composite plates for shape and stiffness control, J. Intell. Mater. Syst. Struct. 19 (2008) 609–619.

[18] C.S. Jarali, S. Raja, Homogenization and pseudoelastic behavior of composite materials reinforced with shape memory alloy fibers, J. Compos. Mater. 42 (2008) 1685–1707.

[19] Y. Freed, J. Aboudi, Thermomechanically coupled micromechanical analysis of shape memory alloy composites undergoing transformation induced plasticity, J. Intell. Mater. Syst. Struct. 20 (2009) 23–38.

[20] S.D. Oehler, D.J. Hartl, R. Lopez, R.J. Malak, D.C. Lagoudas, Design optimization and uncertainty analysis of SMA morphing structures, Smart Mater. Struct. 21 (2012), 094016.

[21] S.M. Khalili, A. Ardali, Low-velocity impact response of doubly curved symmetric cross-ply laminated panel with embedded SMA wires, Compos. Struct. 105 (2013) 216–226.

[22] H. Bahrami, S.H. Hoseini, G.Z. Voyiadjis, Fracture investigation of the shape memory alloy using GTN model, Eng. Fract. Mech. 216 (2019), 106519.

[23] H. Bahrami, S.H. Hoseini, G.Z. Voyiadjis, Fracture analysis of shape memory alloys in martensite and austenite phase based on the voids behavior, Mech. Mater. 137 (2019), 103119.

[24] A.A. Karakalas, T.T. Machairas, D.C. Lagoudas, D.A. Saravanos, Quantification of shape memory alloy damping capabilities through the prediction of inherent behavioral aspects, Shape Mem. Superelasticity 7 (2021) 7–29.

[25] K. Hamada, F. Kawano, K. Asaoka, Shape recovery of shape memory alloy fiber embedded resin matrix smart composite after crack repair, Dent. Mater. J. 22 (2003) 160–167.

[26] X.M. Wang, Y.F. Wang, A. Baruj, G. Eggeler, Z.F. Yue, On the formation of martensite in front of cracks in pseudoelastic shape memory alloys, Mater. Sci. Eng., A 394 (2005) 393–398.

[27] D.S. Burton, X. Gao, L.C. Brinson, Finite element simulation of a self-healing shape memory alloy composite, Mech. Mater. 38 (2006) 525–537.

[28] C. Lexcellent, F. Thiebaud, Determination of the phase transformation zone at a crack tip in a shape memory alloy exhibiting asymmetry between tension and compression, Scripta Mater. 59 (2008) 321–323.

[29] S. Desindes, S. Daly, The small-scale yielding of shape memory alloys under mode III fracture, Int. J. Solid Struct. 47 (2010) 730–737.

[30] C. Maletta, F. Furgiuele, Fracture control parameters for NiTi based shape memory alloys, Int. J. Solid Struct. 48 (2011) 1658–1664.

[31] J.B. Ferguson, B.F. Schultz, P.K. Rohatgi, Zinc alloy ZA-8/shape memory alloy self-healing metal matrix composite, Mater. Sci. Eng., A 620 (2015) 85–88.

[32] A. Cohades, N. Hostettler, M. Pauchard, C.J. Plummer, V. Michaud, Stitched shape memory alloy wires enhance damage recovery in self-healing fibre-reinforced polymer composites, Compos. Sci. Technol. 161 (2018) 22–31.

[33] A. Afshar, A. Daneshyar, S. Mohammadi, XFEM analysis of fiber bridging in mixed-mode crack propagation in composites, Compos. Struct. 125 (2015) 314–327.

[34] M. Karimi, H. Bayesteh, S. Mohammadi, An adapting cohesive approach for crack-healing analysis in SMA fiber-reinforced composites, Comput. Methods Appl. Mech. Eng. 349 (2019) 550–575.

[35] M.M. Mirsayar, D.J. Hartl, On the cracks normal to shape memory alloy/elastic material interfaces, Eng. Fract. Mech. 216 (2019), 106509.

[36] S.H. Ardakani, H. Moslemzadeh, S. Mohammadi, Delamination analysis in bimaterials consisting of shape memory alloy and elastoplastic layers, Compos. Struct. 225 (2019), 111149.

[37] M.M. Mirsayar, D.J. Hartl, On the validity of strain energy density criterion for mixed mode I/II fracture analysis of notched shape memory alloy components, Eng. Fract. Mech. 214 (2019) 270–288.

[38] D. Lagoudas, D. Hartl, Y. Chemisky, L. Machado, P. Popov, Constitutive model for the numerical analysis of phase transformation in polycrystalline shape memory alloys, Int. J. Plast. 32 (2012) 155–183.

[39] D.C. Lagoudas, Shape Memory Alloys: Modeling and Engineering Applications, Springer Science & Business Media, 2008.

[40] Y. Zhang, Y. You, Z. Moumni, G. Anlas, J. Zhu, W. Zhang, Experimental and theoretical investigation of the frequency effect on low cycle fatigue of shape memory alloys, Int. J. Plast. 90 (2017) 1–30.

[41] S. Mohammadi, Extended Finite Element Method: for Fracture Analysis of Structures, John Wiley & Sons, 2008.

[42] S. Bordas, P.V. Nguyen, C. Dunant, A. Guidoum, H. Nguyen-Dang, An extended finite element library, Int. J. Numer. Methods Eng. 71 (2007) 703–732.

[43] S. Natarajan, S. Bordas, D. Roy Mahapatra, Numerical integration over arbitrary polygonal domains based on Schwarz–Christoffel conformal mapping, Int. J. Numer. Methods Eng. 80 (2009) 103–134.

[44] J. Nie, J. Shen, Y. Yuan, General formula for calculating the deformation of steel-concrete simply supported composite beams, Eng. Mech. 11 (1994) 1–7.

[45] J. Nie, J. Shen, Z. Yu, A reduced stiffness method for deformation calculation of steel-concrete composite beams with slip effect, J. Civ. Eng. 28 (1995) 11–17.

[46] C.S. Jarali, D.R. Mahapatra, Modeling the interface effect of shape memory alloy composite materials, Multidiscip. Model. Mater (2010) 257–283.